CHAPTER 1

INTRODUCTION

The study of giant resonances in stable nuclei has been one of the major fields of research in medium-energy nuclear physics since the first systematic investigation of the isovector giant dipole resonance in 1947 [BA47]. Inelastic electron [KU81], proton [LI91] and α-particle [BE81] scattering played an important role in the discovery of such resonances. The strength of the resonance, though, depends on the probe and its incident energy and the scattering angle measured. Several different processes contribute to the shape of the resonance. An important finding recently in the case of the Isoscalar Giant Quadrupole Resonance (ISGQR) in ^{208}Pb was that the shape of the resonance is probe independent [KA97].

The ISGQR can be described as a quadrupole (ΔL = 2) shape vibration of the surface of a nucleus for a prolate form of surface vibration, the protons and neutrons oscillating synchronously, thus defining an isoscalar (ΔT = 0) nature of this resonance. Microscopically, giant resonances are generally described with the help of the random phase approximation (RPA) theories where each separate nucleon is moving in an average mean field potential created by all the other nucleons, but without interacting with any other nucleon. The only way to understand the origin and physical nature of different scales is by comparison of experimentally observed values with model predictions.

This motivated an extensive study of the ISGQR at the cyclotron facility of iThemba LABS using the K600 Magnetic Spectrometer. In particular, this lead to high energy-resolution measurements by development of the techniques used to match the cyclotron beam optics to the optics of the spectrometer [CA02]. Identification of energy scales in high energy-resolution proton inelastic scattering exciting giant resonances in nuclei over a wide range has been studied in [SH04a] and [KA04]. In a novel application of the wavelet analysis technique [SH04a], it was shown that the energy scales extracted from experimental spectra could be related to those determined from microscopic model calculations including two-particle two-hole (2p-2h) degrees of freedom, identifying the coupling to surface vibrations as the main source of the scales observed. This was best achieved within the Quasi-particle Phonon Model (QPM).

The main aim of this Research Report is to analyse the experimental data for ISGQR excitation in a range of close-shell nuclei across the periodic table and to compare the extracted characteristic energy scales with the theoretical QPM using both Fourier and Wavelet analysis. Further insight could then be gained as to the nature of these characteristic energy scales by reconstruction back to the original spectrum using inverse Fourier transform and Wavelet methods.

The layout of this Research Report is as follows:

- Chapter 2 describes the theoretical considerations and methods used to analyse the data.
- Chapter 3 presents the analysis of the experimental data and theoretical predictions and the application of the inverse Fourier transform for the reconstruction of original spectra together with Wavelet methods of reconstruction.
- Chapter 4 presents the conclusions.
- Appendix A is a copy of the recent Physical Review Letters publication which lead to the present investigation.
- Appendix B is an extract from the PhD thesis of A. Shevchenko concerning an extensive discussion of Wavelet techniques for reconstruction using the Discrete Wavelet Transform.

CHAPTER 2

THEORETICAL CONSIDERATIONS

2.1 Introduction

In this chapter the mathematical tools required to extract characteristic energy scales from both the experimental data and the theoretical predictions will be discussed. This model independent analysis will be used in Chapter 3 to ascertain the correspondence between scales observed in the experimental data and the appearance of scales in the theoretical predictions, which in turn can be linked to specific damping processes of the Isoscalar Giant Quadrupole Resonance (ISGQR).

A general description of the excitation and decay of giant resonances is presented in Section 2.2 together with a discussion of the properties of the ISGQR. This is followed by a description of the damping mechanisms associated with giant resonances in Subsection 2.2.1. State-of-the-art calculations of ISGQR excitation and damping are then discussed in Subsection 2.2.2. Tools for extracting characteristic energy scales are presented in Section 2.3 and encompass the use of the Fourier Transform and Wavelet Analysis. Finally, details concerning reconstruction of specific features in the experimental spectra using the Inverse Fourier Transform and Wavelet methods are presented in Section 2.4.

2.2 Excitation of nuclear giant resonances

Giant resonances are simple, collective, one particle-one hole (1p-1h) excitations involving the whole nucleus. Such resonances are elementary modes of nuclear excitation which involve the coherent motion of many nucleons in the nucleus. These oscillations are classified by their angular momentum as monopole (ΔL = 0), dipole (ΔL = 1), quadrupole (ΔL = 2) etc. resonances [BE79]. Each type is subdivided according to isospin, ΔT, and spin, ΔS, transfers as illustrated in Fig. 2.1. The Isoscalar (ΔT = 0) modes are vibrations in which neutrons and protons move in phase. Modes in which neutrons and protons move out of phase are called Isovector (ΔT = 1). Similar oscillations may take place in the spin space.

Nucleons with spin-up and spin-down can move either in phase ($\Delta S = 0$ modes) or out of phase ($\Delta S = 1$ modes). It has been demonstrated that the fine structure of giant resonances may carry the relevant information on the dominant damping mechanism [VO05].

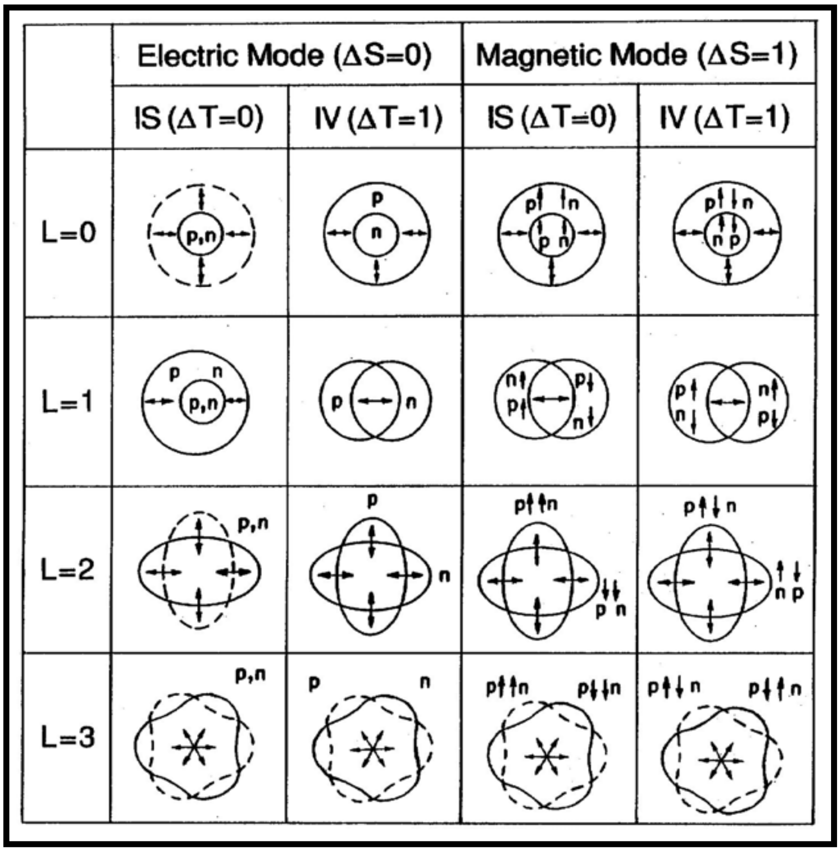

Figure 2.1 Excitation of nuclear giant resonances illustrating the isoscalar and isovector electric and magnetic resonances [IT05].

The effect of ground state surface properties on the shape of giant resonances known as macroscopic picture can be related to the energy splitting which is caused as a result of deformation and the quadrupole moment of the nuclear ground state [VA87]. The concept of the doorway picture explains that the internal mixing occurs through a hierarchy of couplings towards more and more degrees of freedom in the nucleus, starting from the two particle-two hole (2p-2h) states and ending with the *n*p-*n*h states of the compound nucleus [CA90], [RE94], and [AB96].

Collective modes are treated as small-amplitude vibrations around the ground state. These vibrations are described via coherent overlap of many one particle – one hole excitations. A schematic representation of such a microscopic description for the Giant Dipole Resonance (GDR) and the Giant Quadrupole Resonance (GQR) for the example of ^{90}Zr is illustrated in Fig. 2.2, where 1p-1h transitions contribute coherently to a dipole (ΔL = 1) or to a quadrupole (ΔL = 2) mode. Proton (arrows with solid circles) and neutron (arrows with open circles) 1p-1h transitions from and to corresponding energy levels below and above the Fermi level ε_F are shown.

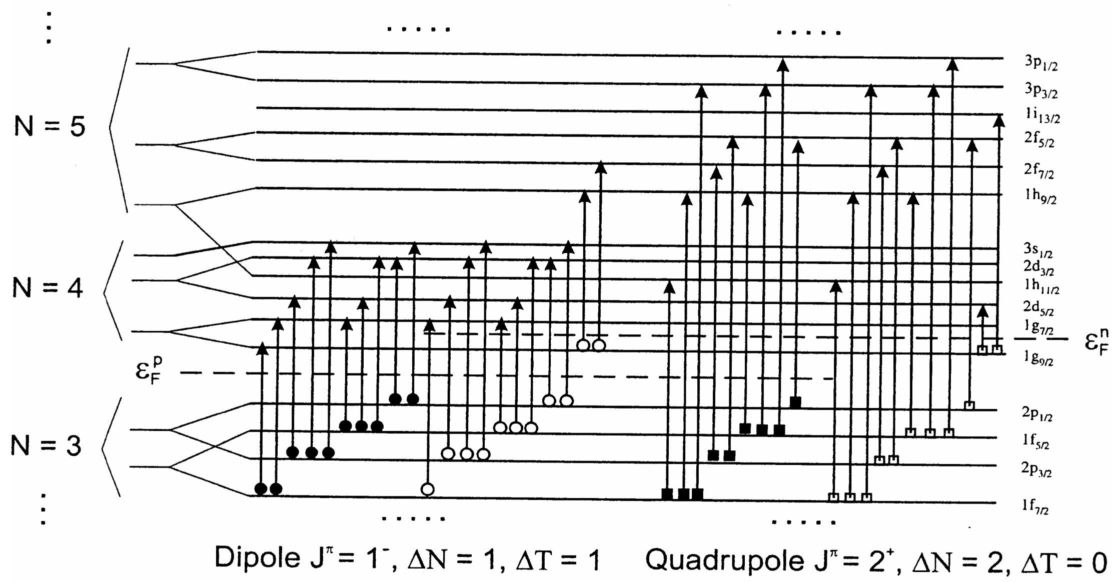

Figure 2.2 Microscopic description of giant resonances for ^{90}Zr (taken from [SH04b]).

2.2.1 Width and decay of Giant resonances

The strength distribution of the various giant resonances in spherical nuclei can be quantitatively described by a Gaussian or Lorentzian function with a width Γ, which is, like the excitation energy E_x, of a smooth function of the mass number A. As a first approximation, the total width Γ can be written as

$$\Gamma = \Delta\Gamma + \Gamma\uparrow + \Gamma\downarrow, \tag{2.1}$$

where $\Gamma\uparrow$ is the escape width, $\Gamma\downarrow$ is the spreading width and $\Delta\Gamma$ is the Landau damping. The Landau damping occurs because not all collective 1p-1h strength, which acts as a doorway for the giant resonance, is necessarily concentrated in one single state but can be already appreciably fragmented. This is true for the higher multipole resonances.

Giant resonances are located, in general, at excitation energies above the particle binding energy so that they will decay predominantly by particle emission, charged particles and neutrons in light nuclei and because of the Coulomb barrier, neutrons only in heavier nuclei. Particle decay can occur through various processes as shown in Fig. 2.3. The coupling of the (1p-1h) state to the continuum gives rise to semi-direct decay into the hole states of the (A-1) nucleus with a partial width $\Gamma\uparrow$, the escape width. If this process is the only one populating the hole state, then the relative population of these states would reflect the microscopic structure of the giant resonance. Also, the spreading width $\Gamma\downarrow$ arises as result of the (1p-1h) doorway state which is mixed through the residual interaction with the more complicated and numerous (2p-2h) states which are present in the vicinity of the resonance.

Figure 2.4 illustrates the results of (α,α') experiments demonstrating the prominent excitation of the ISGQR [BE81] as a Lorentzian shape. With advancement in experimental techniques, more intrinsic structure can be found with high energy resolution experiments. It should in particular be noticed that as target mass increases the ISGQR becomes considerably more compact and moves to lower excitation energy.

One assumption often made is that the (2p-2h) states couple again to (3p-3h) …..(np-nh) states till finally a completely equilibrated system is reached. Particle

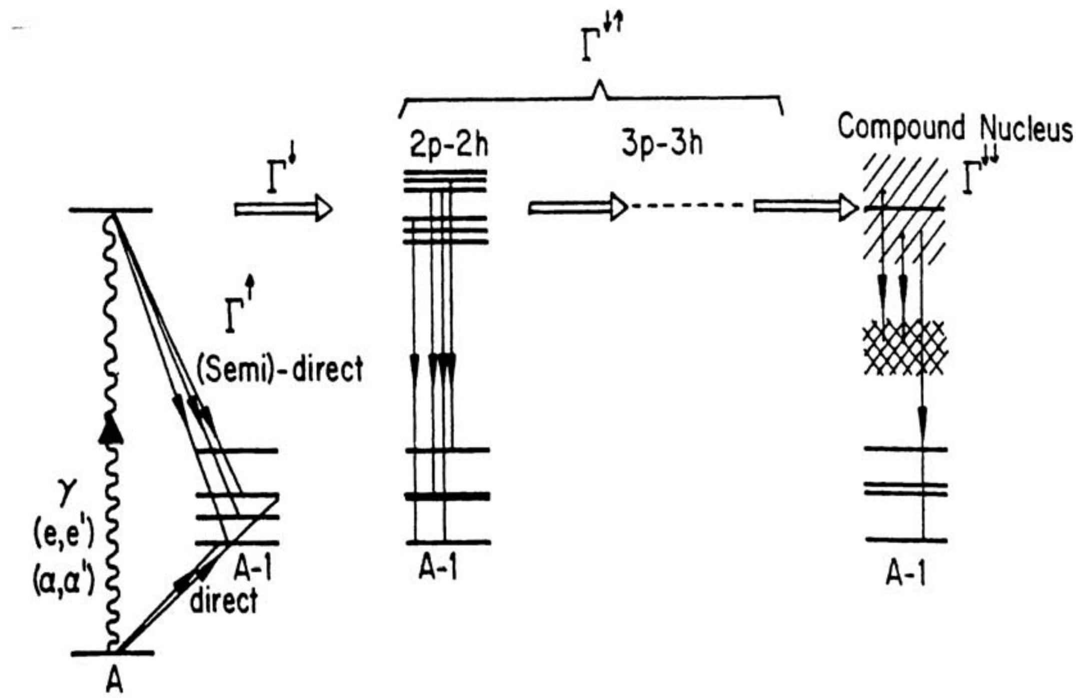

Figure 2.3 Schematic representation of the various nucleon decay modes of a giant resonance (taken from [VA87]).

decay can occur at each intermediate level. For a fully equilibrated system, the decay system, the decay will be similar to that of a compound nucleus with the same excitation energy, spin and parity as the giant resonance. The total spreading width is given by

$$\Gamma\downarrow = \Gamma\downarrow\uparrow + \Gamma\downarrow\downarrow, \tag{2.2}$$

where $\Gamma\downarrow\uparrow$ is the partial width for pre-equilibrium decay and $\Gamma\downarrow\downarrow$ for statistical decay. In the case of the ISGQR it was found that, for a range of closed shell nuclei between ^{40}Ca and ^{208}Pb, damping into the doorway states (particle-hole + vibration) accounts for about 60% of the experimental width [BE83].

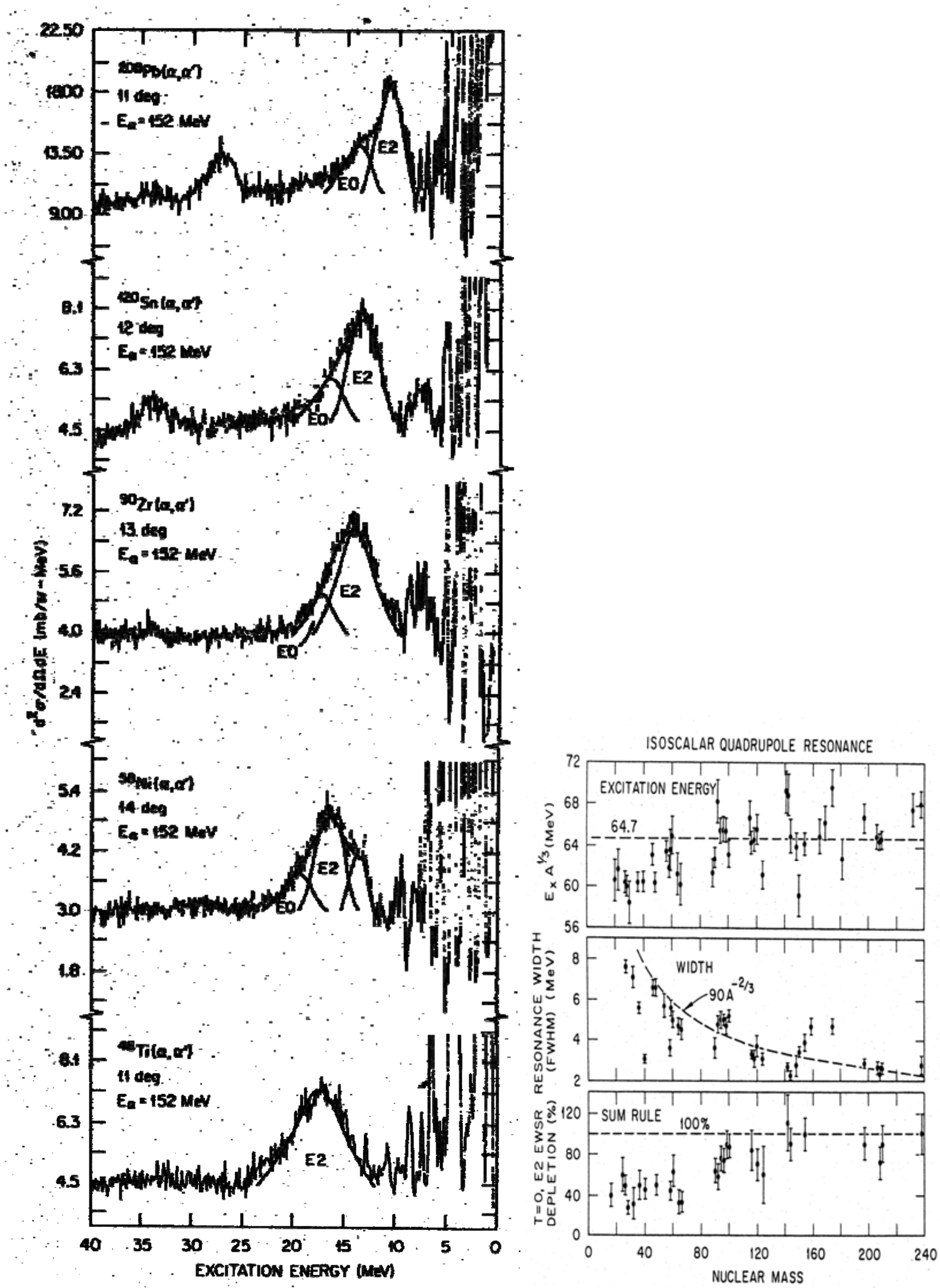

Figure 2.4 Systematics of GQR across the periodic table showing the variations in excitation energy, width and sum rule (taken from [BE81]).

2.2.2 Theoretical interpretation of giant resonances

For a physical interpretation of experimental results obtained one has to compare them with the microscopic predictions of the strength functions generated by different models. Such models include Quasi-particle Phonon Model (QPM) [BE99], Random Phase Approximation (RPA) [RO70], Second-RPA (SRPA) [LA00], Extended Theory of Finite Fermi Systems (ETFFS) [KA97] and Extended Time Dependent Hartree-Fock (ETDHF) [LA01].

An important mechanism contributing to the damping of the single-particle as well as the collective response in heavy nuclei is the coupling to low-lying surface vibrations, termed Collective, and on the other hand, significant contributions also come from mixing of the initial 1p-1h states with the large background of states with more complex wave functions, termed Non-collective. These two contributions have clearly identifiable contributions in the QPM model which gives the best correspondence to the measured experimental spectra [SH04a].

Experimental achievements demand a theoretical treatment of giant resonances on an equivalent level. For this reason, Quasi-particle Phonon model has been used for the microscopic analysis of states forming giant resonances as well as low-lying states [VO83]. The model Hamiltonian $\mathcal{H}$ includes an average field $V_{p(n)}$ for protons and neutrons, a monopole pairing interaction and isoscalar and isovector residual interaction of a separable type with a form factor proportional to $dV_{p(n)}/dr$. Excited states of even-even nuclei are treated in terms of phonon excitations built upon the ground state that is considered as a phonon vacuum $|0\rangle_{ph}$ [PO93].

2.3 Tools for extracting energy scales

2.3.1 Fourier Transform

Fourier analysis as a signal processing tool has had extra-ordinary success in many different scientific fields. Typically, it is applied to a time-sequence data set to determine dominant periodicities from the power spectrum extracted. In this Research Report, both the experimentally measured data from inelastic proton scattering and the theoretical predictions of the QPM were analysed using the Fourier transform. In each case, standard data preparation techniques were applied in order to avoid spurious end effects. However, a shortcoming of Fourier analysis is that scales cannot be identified directly in specific regions of the energy spectrum analysed.

The Fast Fourier Transform is a perfectly general mathematical transformation which was developed many years ago. This powerful tool relies on its ability to relate some very important pairs of physical variables, the most important of which are probably those of time and frequency [DE84]. As such, it is possible to transform the present results obtained as a function of energy and express them either as a function of frequency or as a function of wavelength (1/frequency) in the corresponding energy units.

2.3.1.1 Discrete Fourier Transform

Given an input data sequence of length N the Discrete Fourier Transform (DFT) is defined as $X(k)$ and is given by

$$X(k) = \sum_{n=1}^{N} x(n) \exp(-2\pi i)(k-1)\left(\frac{n-1}{N}\right) \quad 1 \le k \le N \ . \tag{2.3}$$

Here, $X(k)$ are referred to as the Fourier coefficients or harmonics. Both $x(n)$ and $X(k)$ are, in general, complex. Also, the sequences $x(n)$ and $X(k)$ are referred to as "time domain" and "frequency domain" data, respectively. In principle, of course, there is no reason why $x(n)$ should be a sampled time series. The present case uses a signal which is a function of energy as the input data sequence. The above equation was computed in Matlab [MA06] using a Fast Fourier Transform (FFT) algorithm.

2.3.1.2 Periodogram

The periodogram for a sequence $[X_1, \ldots, X_n]$ is given by the following formula:

$$S\left(e^{i\omega}\right)=\frac{1}{n}\left|\sum_{l=1}^{n} x_l e^{-i\omega l}\right|^2 . \tag{2.4}$$

This expression forms an estimate of the power spectrum of the signal defined by the sequence $\left[X_1,\ldots,X_n\right]$. If the signal sequence is weighted by a window $\left[w_1,\ldots,w_n\right]$, then the weighted or modified periodogram is defined as [WE67]

$$S\left(e^{i\omega}\right)=\frac{1}{n}\left|\sum_{l=1}^{n} x_i e^{-i\omega l}\right|^2 \Bigg/ \frac{1}{n}\sum_{l=1}^{n}\left|w_l^2\right| . \tag{2.5}$$

In either case, periodogram uses an n-point FFT to compute the power spectral density as $S\left(e^{i\omega}\right)/F$, where F is 2π when the sampling frequency was not supplied and f_s when the sampling frequency was supplied, with f_s as the given sampling frequency.

2.3.1.3 Power spectrum

In the case of a time series the result of the Fourier transform is a complex vector. The absolute value of the complex vector is called the power P, and is given by the expression below as:

$$P=\sqrt{\left(\operatorname{Re} X(k)\right)^2+\left(\operatorname{Im} X(k)\right)^2} . \tag{2.6}$$

Here, 1/frequency was used to obtain wavelength from an energy spectrum so as to provide a power spectrum against a characteristic scale in units of energy (keV or MeV).

2.3.1.4 Input Data Preparation

Standard techniques have been developed in order to minimize end effects due to a limited input data set and the resulting spurious Fourier coefficients.

- Subtraction of the dataset mean: the mean of the input data set is subtracted from the data set in order to reduce the size of the discontinuity at the start and end of the data set.
- Zero padding to 2^m data points: leading and trailing zeros are added to the input data set to produce a vector of length $2^m = N$, the next highest integer multiple of 2.
- Hamming window: in both digital filter design and power spectrum estimation, the choice of a windowing function can play an important role in determining the quality of overall results. The main role of the window is to damp out the effects of the Gibbs phenomenon that results from truncation of an infinite series. The Hamming window is a special case of the generalized cosine window. The coefficients of a Hamming window are computed from the following equation

$$w(n) = 0.54 - 0.46\cos\left(2\pi \frac{n}{N}\right) \qquad 0 \le n \le N\,, \tag{2.7}$$

  where N is the window length.
- Cosine bell: finally a cosine bell is applied to the padded portion of the data.

2.3.2 Wavelet analysis

Wavelet analysis of the input data set allows not only the “energy scales” of the input excitation energy spectrum to be determined but also the position of the scales within the energy spectrum. There are basically two classes of wavelet transform: Continuous Wavelet Transform (CWT) and Discrete Wavelet Transform (DWT).

2.3.2.1 Continuous Wavelet Transform (CWT)

The Continuous Wavelet Transform (CWT) is defined as the sum over all time of the signal multiplied by a scaled, shifted version of the wavelet function Ψ, which can be expressed as

$$C(a,b) = \int S(t) \frac{1}{\sqrt{a}} \psi \left\{ \left(\frac{t-b}{a} \right) \right\} dt \quad , \tag{2.8}$$

where a is the scale and b is the position and are equivalent to δE and E_x, respectively, in the analysis of energy scale. By folding the original energy spectrum $\sigma(E)$ with a chosen wavelet function Ψ, the coefficients are obtained as

$$C(E_x, \delta E) = \frac{1}{\sqrt{\delta E}} \int \sigma(E)\, \psi \left(\frac{E_x - E}{\delta E} \right) dE \,. \tag{2.9}$$

The parameters (excitation energy E_x and bin size δE) can be varied continuously or in discrete steps j, where $\delta E = 2j$, $j = 1, 2, 3$ …, and $E_x = \delta E$. A variety of wavelets provides a set of tools for performing many different tasks. The choice of wavelet is made based on its mathematical properties among of which are moments, compact support (which obeys the uncertainty principle), regularity of a signal (the number of times that it is continuously differentiable), to mention a few. Complex wavelets produce complex CWT coefficients, allowing the phase of the result to be examined. The general principles of wavelet analysis and wavelet function representations are shown in Fig. 2.5.

Generally, the wavelet transform has been proven to be useful for analysing signals which can be characterised as periodic, noisy, intermittent, irregular, transient or fractal to mention a few. Examples of wavelet functions are:

a) The Haar wavelet which is just a step function and used in entropy index analysis.
b) Mexican Hat is the second derivative of a Gaussian.
c) Real and Complex Morlet wavelets are the products of cosine and Gaussian functions.
d) The Biorthogonal 3.9 wavelet has an antisymmetrical shape but no analytical expression.

The Morlet wavelet function best approximates to the measured energy spectra with peaks generally well described by a Gaussian function.

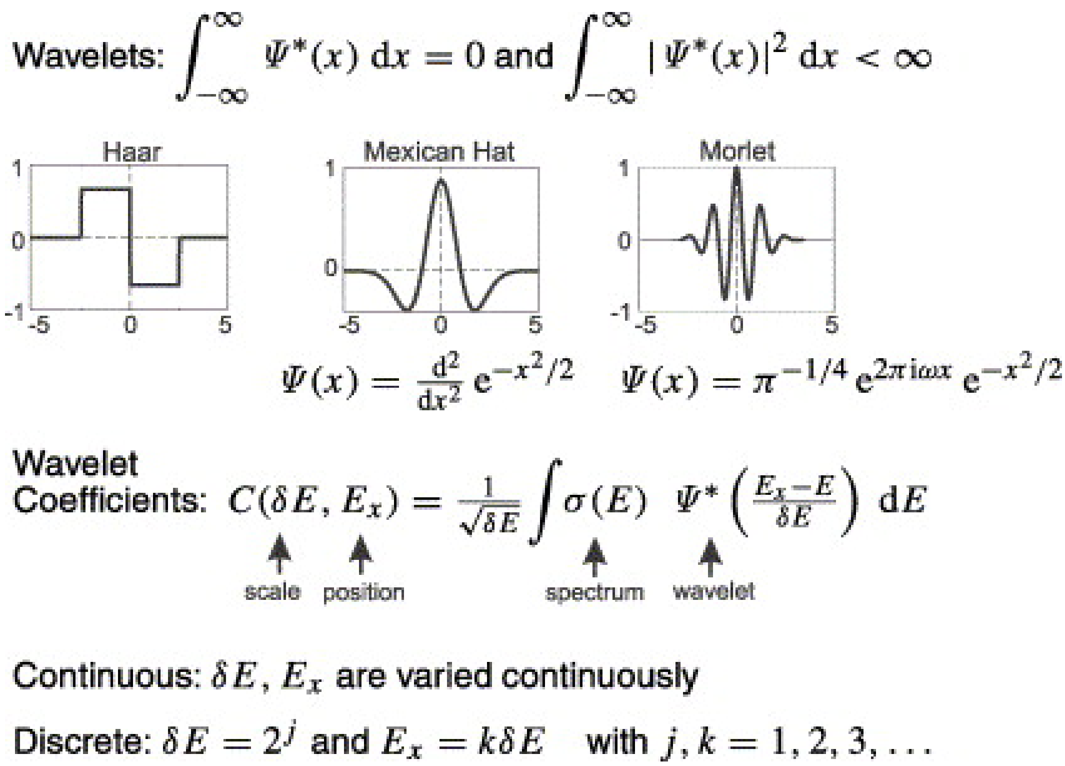

Figure 2.5 Illustration of the principles of wavelet analysis and wavelet function representations (taken from [KA94]).

In the present case a continuous Wavelet analysis is performed using a specific wavelet function of the complex version of the Morlet wavelet family given by:

$$\psi(x) = \frac{1}{\sqrt{\pi f_b}} \exp(2\pi i f_c) \exp\left(-\frac{x^2}{f_b}\right), \tag{2.10}$$

where f_c is the wavelet centre frequency and f_b is the band-width parameter. In addition, the real Morlet wavelet is derived by taking a periodic wave and by localizing it with a Gaussian envelope and is expressed as

$$\psi(x) = \frac{1}{\pi^{1/4}} \exp(2\pi i \omega x) \exp\left(-\frac{x^2}{2}\right). \tag{2.11}$$

Wavelets can be used to compute derivatives of different orders. The number of vanishing moments of a wavelet indicates the order of the derivative that it will determine. Computation of derivatives is equivalent to smoothing the data using the scaling function of the wavelet before performing the derivative calculation. The width of the wavelet used controls the amount of the smoothing. The derivative is determined from the coefficients of the CWT at a particular scale. Meanwhile, it is important to note that the choice of wavelet used also affects the amount of smoothing at a given level.

2.3.2.2 Discrete Wavelet Transform (DWT)

The Discrete Wavelet Transform (DWT) is a more efficient way of representing data than the CWT and as such is better suited to applications such as compression and filtering. A disadvantage of the DWT is that it is not shift-invariant i.e. the DWT of a signal and a shifted version of itself are not shifted versions of each other. Another disadvantage of the DWT is that it is configured in powers of 2. From the CWT equation, Eq. (2.8), if *a* and *b* assume only discrete values then from Eq. (2.9)

$$\delta E_k = 2^k \Delta \quad \text{and} \qquad E_{xk} = k.\delta E_k,\ \ k = 1, 2, \ldots.., \tag{2.12}$$

where Δ is the bin size of the data. Here, the value of k specifies the number of significant sinusoidal oscillations within a Gaussian window. Details of this method are reproduced from [SH04b] in Appendix B and it has been used here only for comparison purposes.

2.3.2.3 Input data preparation and power spectra

It should also be emphasised that, as in Fourier analysis, input data preparation is absolutely essential in order to minimize end effects. The procedures of Subsection 2.3.1.4 can be followed but not including the Hamming function. However, after initial testing it was found sufficient to subtract the mean of the data from the data before applying the wavelet technique. It should be noted that the extracted energy scales from a Wavelet analysis using a Complex Morlet wavelet are directly comparable to energy scales obtained from a Fourier analysis. This is not, however, the case when a real Morlet wavelet is used where energy scales obtained from the corresponding power spectrum have to be divided by a factor of 0.813 in order to yield scales directly comparable to the Fourier scale.

Two dimensional plots are produced from the wavelet coefficients - scale *versus* excitation energy (see for example the coefficient plots of Fig. 3.7). Plotted, however, are the real coefficients of the Complex Morlet complex coefficients - the positive and negative parts allowing spectrum reconstruction later. But the power spectrum is obtained from the complex coefficients. Significant power resides in the imaginary part, especially for larger scales.

2.4 Reconstruction of the Original Spectrum

2.4.1 Inverse Fourier Transform

The Fourier transform calculates a signal's frequency domain representation from its time (energy)-domain variant while the Inverse Fourier transform finds the time (energy)-domain representation from the frequency domain. The Fourier transform of function *f(t)* is given as

$$f(\omega) = \int_{-\infty}^{\infty} f(t) e^{-i\omega t} dt . \tag{2.13}$$

For a sufficiently smooth *f (t)* we can recover *f(t)* at any point *t* of continuity from the transform $f(\omega)$ as

$$f(t) = \frac{1}{2\pi} \int_{-\infty}^{\infty} f(\omega) e^{i\omega t} d\omega . \tag{2.14}$$

In this case, both the Fourier transform and its inverse are continuous and decay to zero as $\omega \to \infty$ [GE00]. In most cases, $1/2\pi$ is used in front of the transform to produce a symmetric appearance.

The technique of Fast Fourier Transform lends itself to the filtering of the original spectrum. By including all of the Complex Fourier coefficients an exact reconstruction of the original spectrum is possible. However, in the case of the giant quadrupole resonance investigated here it is useful to gain insight into the specific structures generated by the different energy scales identified. This can be done by the application of suitable filters to the Fourier coefficients before applying the inverse Fourier transform. A basic method used to reconstruct a band limited signal from its samples on the integer is by turning the sample sequence into an impulse train and then a low-pass filter is applied to the pulse train to get the reconstruction f(t) back by setting the appropriate cutoff frequency.

2.4.2 Spectrum reconstruction from Wavelet analyses

It is possible to reconstruct the original signal from the coefficients generated by both the Discrete Wavelet Transform (DWT) and the Continuous Wavelet Transform (CWT). However, the limited scales resolution (factors of 2) of the DWT motivated the use of the CWT for a new method of spectrum reconstruction in the present analysis.

2.4.2.1 Discrete wavelet transform reconstruction

The Discrete Wavelet Transform (DWT) is used to analyse or decompose signals and images. This process is called decomposition or analysis. Those components can be assembled back into the original signal without loss of information. This process is called reconstruction or synthesis. The wavelet is determined from the differencing coefficients *h(k)* using the wavelet equation

$$\psi(t) = 2\sum_{k=0}^{N} h(k)\Phi(2t-k), \qquad (2.15)$$

where ψ represents the wavelet (high-pass filter) and Φ represents the scaling function, which is generated by high-pass and low-pass filter coefficients.

The DWT breaks the data down into a sequence of approximations and details by using low-pass and high-pass filters. The mathematical manipulation that affects synthesis is called the inverse discrete wavelet transform. The process is repeated to yield a multilevel decomposition. It is important to note that the low-pass portion of the data is decomposed repeatedly rather than the high-pass filtered portion because in most datasets it contains the majority of the energy (see Appendix B).

2.4.2.2 Continuous wavelet transform reconstruction

The Continuous Wavelet Transform (CWT) employing a complex Morlet wavelet was used for reconstruction of the original experimental spectrum. Such a reconstruction has the advantage over the DWT method (constrained to powers of 2 of the energy scale) that any particular scale or set of scales can be chosen for the reconstruction process. This allows large or small scales to be specifically selected. Details of the method are presented in Subsection 3.5.2.

CHAPTER 3

ANALYSIS OF ENERGY SCALES IN THE ISOSCALAR GIANT QUADRUPOLE RESONANCE

3.1 Introduction

In this chapter, the high energy-resolution data from inelastic proton scattering measured at the iThemba LABS cyclotron facility for the closed-shell nuclei ^{208}Pb, ^{120}Sn, ^{90}Zr, and ^{58}Ni are analysed using both Fourier Transform and Wavelet Analysis techniques. The characteristic energy scales of the Isoscalar Giant Quadrupole Resonance (ISGQR) obtained are compared with those obtained from the theoretical model calculations. Reconstruction of specific features in the ISGQR energy spectrum then follows in order to gain further insight into the details of the resonance.

3.2 Measured Experimental Data

A series of measurements [CA02] has been performed at the cyclotron facility of iThemba LABS using the K600 Magnetic Spectrometer to search systematically for the energy scales of the ISGQR. Data were taken for the closed-shell nuclei ^{208}Pb, ^{120}Sn, ^{90}Zr, and ^{58}Ni with an energy resolution $35 \leq \Delta E \leq 50$ keV (FWHM) and for kinematics where the ISGQR is enhanced. An overview of the measured data is given in Table 3.1.

Table 3.1 Data measured at different scattering angles for the targets specified for E_p = 200 MeV. Angles shown in bold denote the maximum of the ISGQR. Note, for clarity only integer values of scattering angles are referred to in the figures.

Target	Scattering Angles
^{208}Pb(Z = 82 , N = 126)	6°, **8°**,10°,12.5°
^{120}Sn(Z = 50, N = 70)	**8°**
^{90}Zr(Z = 40 , N = 50)	**9.2°**, 11°, 13°
^{58}Ni(Z = 28 , N = 30)	**10°**

In proton inelastic scattering a certain kind of multipole mode can be chosen to be rather selectively excited for the appropriate kinematics conditions. The scattering angles were chosen to match the maximum of the cross sections for $\Delta L = 2$ excitations in the corresponding targets, thereby exciting predominantly the ISGQR under investigation. This is illustrated in Fig. 3.1 for the case of ^{90}Zr showing a maximum at 9° scattering angle and for ^{208}Pb at 8° scattering angle. It can be seen from this figure that beyond the first maximum of the $\Delta L = 2$ cross-section the maxima of higher-order multipoles start to become significant.

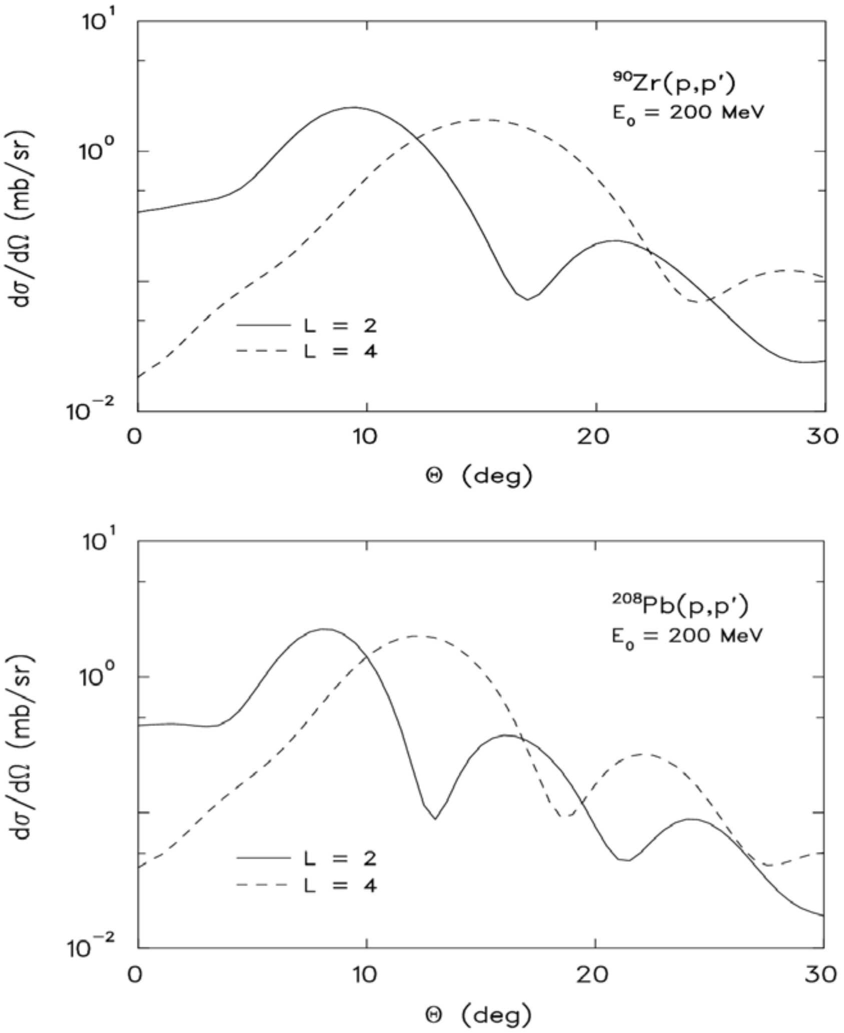

Figure 3.1 Inelastic scattering cross-sections for $\Delta L = 2$ and $\Delta L = 4$ excitations at $E_x = 15$ MeV in ^{90}Zr and ^{208}Pb calculated in the DWBA for an incident proton energy of 200 MeV (taken from [CA02]).

This "Spin-filter" effect was taken advantage of in order to take measurements at and close to the maximum of ISGQR (see Table 3.1). The measured data for each of the target nuclei at the corresponding maximum of ISGQR are show in Fig. 3.2 for the full energy-bite of K600 Magnetic Spectrometer, $6 \leq E_x \leq 22$ MeV (for experimental details see [SH04]). The position and width of the ISGQR for each nucleus is indicated in the corresponding energy spectrum. It should be noted that the systematics of ISGQR were investigated and quantified many years ago (see Subsection 2.2.1 [BE79]). Here it was found that the width of the ISGQR becomes smaller and the resonance moves to a lower excitation energy as the mass of the nucleus increases.

As seen in Fig. 3.2, the ISGQR for ^{208}Pb is very compact with a FWHM of approximately 2 MeV and has a mean energy of $E_x \approx 10.5$ MeV while the ^{58}Ni investigated has a much larger width, FWHM approximately 4 MeV, and a mean energy of $E_x \approx 16$ MeV. Each of the energy spectra displays very different specific details within the region of the ISGQR indicated.

3.3 Experimental Data Analysis

One major aim of this research project was to extract characteristic energy scales of the ISGQR. In order to quantitatively investigate the observed structures, both Fourier and Wavelet analysis techniques were used in extracting the energy scales.

3.3.1 Review of experimental data

Inelastic-scattering excitation energy spectra were measured at and close to the scattering angle corresponding to the maximum cross-section for $\Delta L = 2$ excitations in various closed-shell target nuclei across the periodic table. The experimental data are shown on the left hand side of Figs. 3.3, 3.4, 3.5 and 3.6 for ^{208}Pb, ^{120}Sn, ^{90}Zr and ^{58}Ni, respectively. Dealing with each target nucleus in turn.

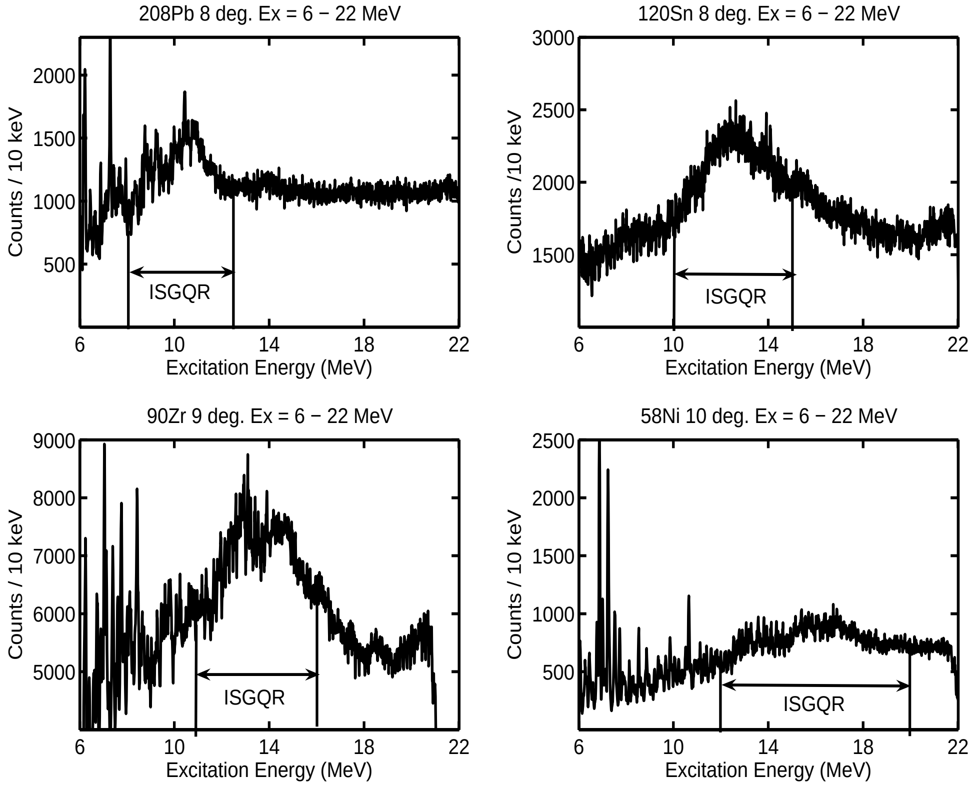

Figure 3.2 Experimentally-measured excitation energy spectra of the ISGQR in several nuclei for E_p = 200 MeV for scattering angles corresponding to a maximum in the E2 cross section. The position and width of the ISGQR is indicated for each nucleus.

^{208}Pb: The excitation energy spectra for ^{208}Pb between 8 and 13 MeV measured at the four different scattering angles are presented in Fig. 3.3. The spectrum at $\theta = 8°$, which is the maximum of the ISGQR, exhibits a distinctive broad peak structure, centred $E_x \approx 11$ MeV and with a width of about 3 MeV. It should be noted that this is very reminiscent of the corresponding structure seen in (α,α') scattering shown in Fig. 2.4. At the larger scattering angles of $\theta = 10°$ and $\theta = 12°$ the broad structure is successively reduced in size and importance but it should be noticed that some of the distinctive fine structure still persists. At the smaller scattering angle $\theta = 6°$ the broad peak structure is lost with a significant rise in the spectrum at larger excitation energies.

^{120}Sn: The experimental data for ^{120}Sn are unfortunately less extensive, with only a single spectrum at $\theta = 8°$ shown in Fig. 3.4, again corresponding to the maximum of the ISGQR. Here, a broad peak at width approximately 3 MeV is observed but centred at somewhat higher excitation energy of $E_x \approx$ 12.5 MeV in comparison to ^{208}Pb. This is consistent with the corresponding feature identified in Fig. 2.4 for (α,α') scattering for ^{120}Sn.

^{90}Zr: In the case of ^{90}Zr three measurements are available, one for $\theta = 9°$ (at the maximum of the ISGQR) and two at larger scattering angles $\theta = 11°$ and $\theta = 13°$ as seen in Fig. 3.5. Here, the ISGQR appears as a broad feature with distinctive sub-structure and a mean energy of $E_x \approx 14$ MeV, consistent with the corresponding peak identified in Fig. 2.4 for (α,α') scattering. The resonance appears to lose strength as expected at the larger scattering angles but again some fine details can still be observed in various regions persisting up to $\theta = 13°$.

^{58}Ni: Data for the lightest nucleus are shown in Fig. 3.6 but only for the $\theta = 10°$ where the ISGQR is predicted to be strongest. Again, a very broad peak can be identified, about 4 MeV wide, being centred at $E_x \approx 16$ MeV, following the trends exhibited by (α,α') scattering in Fig. 2.4.

Thus, a generally good correspondence between the trends and systematics of the ISGQR exists between the (α,α') and (p, p′) scattering data.

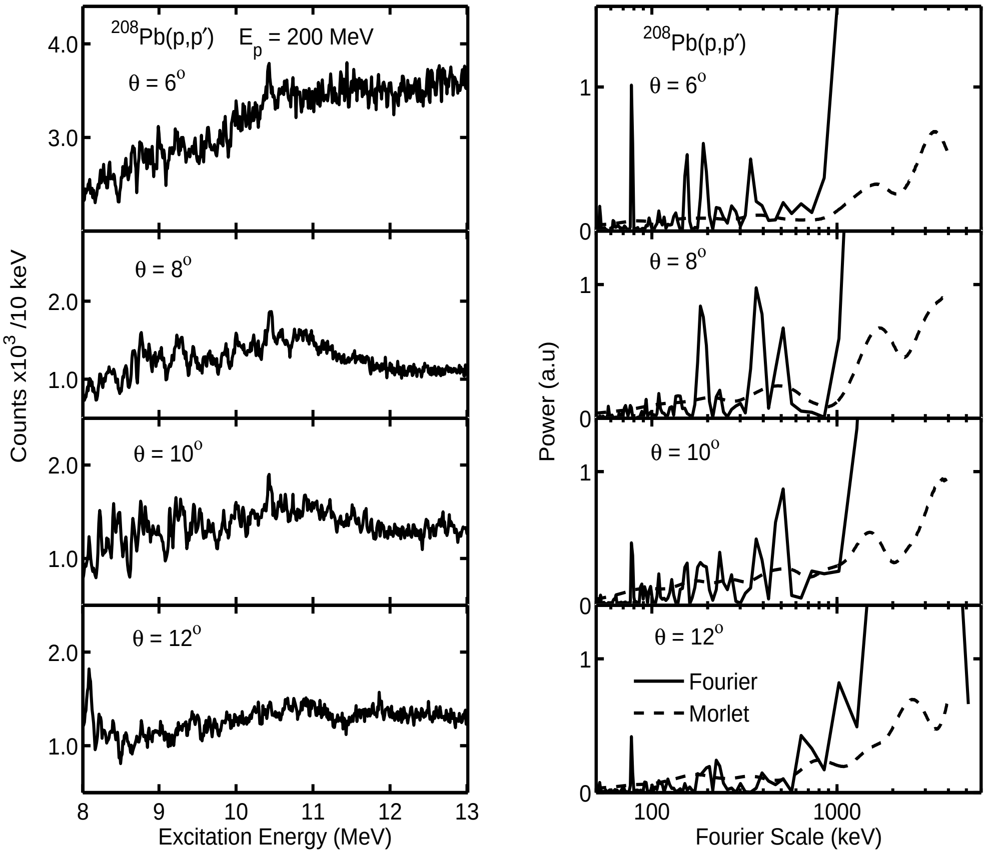

Figure 3.3

Left hand side: Excitation energy spectra in the ^{208}Pb nucleus for different proton scattering angles at E_p = 200 MeV. A scattering angle of θ = 8° corresponds to the maximum of ISGQR cross section.

Right hand side: Corresponding Fourier and wavelet power spectra.

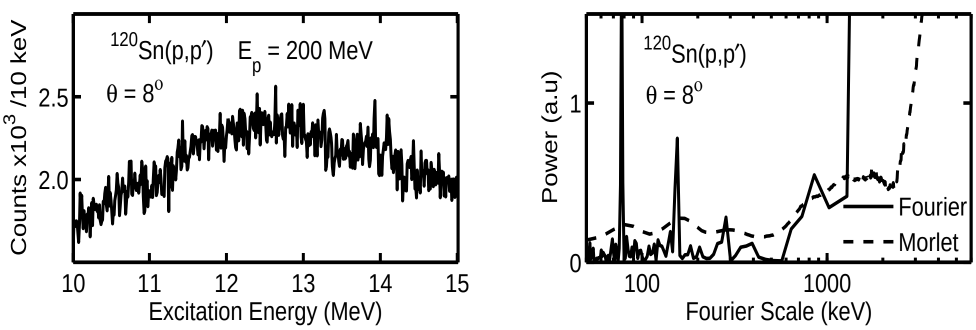

Figure 3.4 As for Fig. 3.3 but for ^{120}Sn with θ = 8° for maximum of ISGQR.

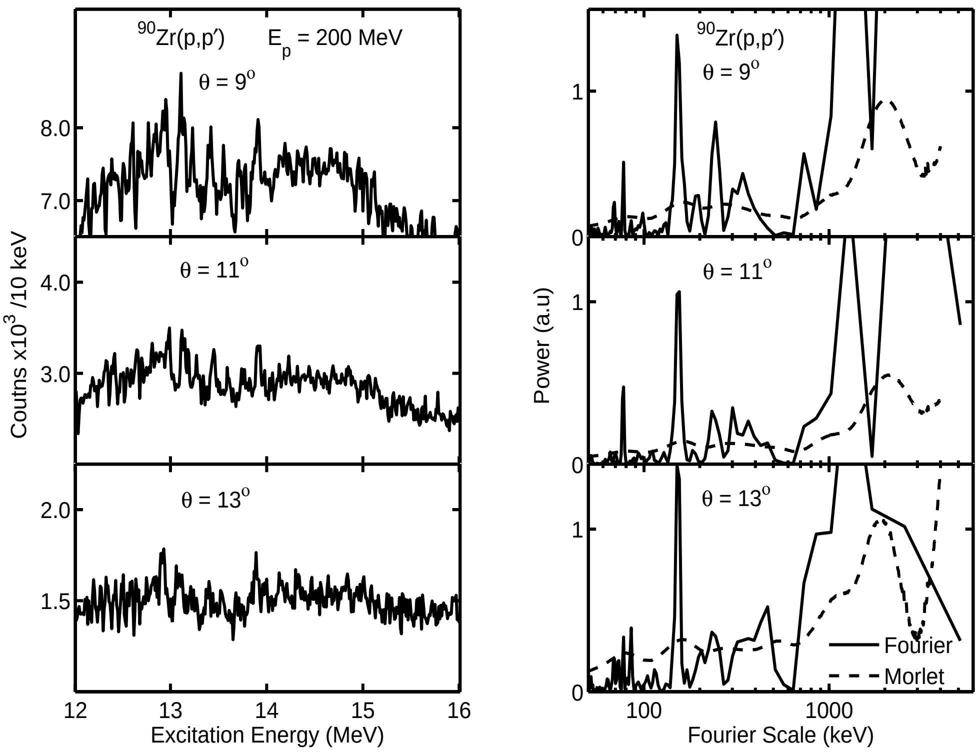

Figure 3.5 As for Fig. 3.3 but for ^{90}Zr with θ = 11° for maximum of ISGQR.

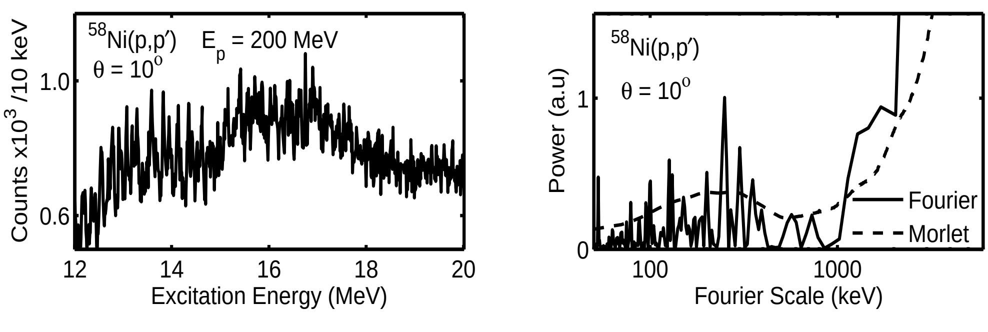

Figure 3.6 As for Fig. 3.3 but for ^{58}Ni with θ = 10° for maximum of ISGQR.

3.3.2 Fast Fourier Transform (FFT)

In this section the regions corresponding to the ISGQR in the measured experimental energy spectra for the closed-shell nuclei ^{208}Pb, ^{120}Sn, ^{90}Zr and ^{58}Ni are analysed using the Fourier Transform.

3.3.2.1 Application of the fast Fourier transform

Energy scales were extracted from the experimental data by applying standard data preparation techniques as discussed in Sub-section 2.3.1.4 in order to minimize reflections and spurious effects before applying the Fast Fourier Transform (FFT) of Eq. (2.3). The standard plot of power *versus* frequency is called a "periodogram" (see Sub-section 2.3.1.2). However, since energy scales are of specific interest in the investigation, power spectra will be shown as power *versus* 1/frequency, yielding directly a wavelength or energy scale. The resulting periodograms are shown as the solid lines in the right hand side of Figs. 3.3, 3.4, 3.5 and 3.6 for ^{208}Pb, ^{120}Sn, ^{90}Zr and ^{58}Ni, respectively.

3.3.2.2 Fourier energy scales

Details of the various power spectra produced after application of the Fast Fourier transform to the experimental data can now be examined. Dealing with each target nucleus in turn.

^{208}Pb: The resulting periodograms for the ^{208}Pb data are shown by the solid lines on the right hand side of Fig. 3.3. At $\theta = 8°$, corresponding to the maximum of the ISGQR, three dominant scales appear below 1 MeV. These scales become less significant on either side of the $\theta = 8°$ scattering angle. There are no specific features to be seen in the periodograms for scales larger than 1 MeV but it will be shown later that these Fourier coefficients are responsible for reproducing the gross structure of the data corresponding to the width of the excitation energy window.

^{120}Sn: The periodogram corresponding to ^{120}Sn at the maximum of the ISGQR, $\theta = 8°$, is shown on the right hand side of Fig. 3.4. Here, various strong scales can be identified below 1 MeV, reaching as low as 80 keV. Again, scales greater than 1 MeV can be attributed to gross features within the excitation energy window.

^{90}Zr: Data at three scattering angles are available for ^{90}Zr and the corresponding periodograms are shown on the right hand side of Fig. 3.5. At the maximum of the ISGQR for $\theta = 9°$ again several distinct scales can be observed below 1 MeV, some of which persist to the larger scattering angles. Scales above 1 MeV again contribute to gross structure within the excitation energy window as for the other nuclei studied.

^{58}Ni: Data taken at the maximum of the ISGQR, $\theta = 10°$, for ^{58}Ni has the resulting periodogram shown on the right hand side of Fig. 3.6. Here, many significant scales can be identified below 1 MeV reflecting the complexity of the measured data. The gross structure of the data again lies in scales above 1 MeV.

On inspection, it can be seen that for each target nucleus different specific scales can be identified in the corresponding periodograms. Generally though, predominant scales at the maximum of the ISGQR tend to die away at scattering angles nearby where measurements are available.

3.3.3 Wavelet analysis

In order to gain more insight as to the position of specific structures associated with specific energy scales in the measured ISGQR data, a Wavelet analysis was performed. The choice and suitability of wavelet function was explored extensively by A. Shevchenko [SH04b]. However, in the present analysis a Complex Morlet function was chosen (see Subsection 2.3.2) since the resulting energy scales extracted are directly comparable to those obtained from the Fourier analysis. It should be noted, however, that in a previous analysis [SH04a] a real

Morlet wavelet was used but in this case extracted scales need to be divided by a factor of 0.813 in order to yield a comparable Fourier scale.

3.3.3.1 Application of Wavelet analysis

The procedures outlined in Subsection 2.3.2.1 were applied to the region in each energy spectrum corresponding to the maximum of the ISGQR for each nucleus studied. The complex Morlet wavelet was applied to the data, thus allowing a direct comparison to be made with the Fourier scale. However, by plotting the real part only of the complex coefficients on a two-dimension plot of scales *versus* excitation energy, the positions of the structures within the original energy spectrum can be identified. This is illustrated in Fig. 3.7 for each of the nuclei studied. Here, the red corresponds to a large positive coefficient (peak maximum) and the blue to large negative (peak minimum) when projected on to the excitation energy axis. As can be seen, the coefficient plots differ significantly except for the largest scale.

3.3.3.2 Wavelet energy scales

In order to obtain the corresponding power spectrum for each nucleus the absolute values of the complex coefficients are summed across onto the scale axis (see Subsection 2.3.2.3). The resulting power spectra are shown as the dashed lines on the right hand side of Figs. 3.3, 3.4, 3.5 and 3.6 for ^{208}Pb, ^{120}Sn, ^{90}Zr and ^{58}Ni, respectively. Dealing with each target nucleus in turn.

^{208}Pb: The dashed lines shown on the right hand side of Fig. 3.3 correspond to the power spectra obtained from a Wavelet analysis of the ^{208}Pb data. At $\theta = 8°$, the maximum of the ISGQR, two peaks can be identified below a scale of 1 MeV. It should be noted though that the position of these peaks corresponds to peaks in the periodogram where significant power resides. Above a scale of 1 MeV a peak can be identified at approximately 1.7 MeV which persists at the other scattering angles. In addition, there is the indication of a peak at a scale of approximately 4 MeV also persisting at the angles on either side of $\theta = 8°$.

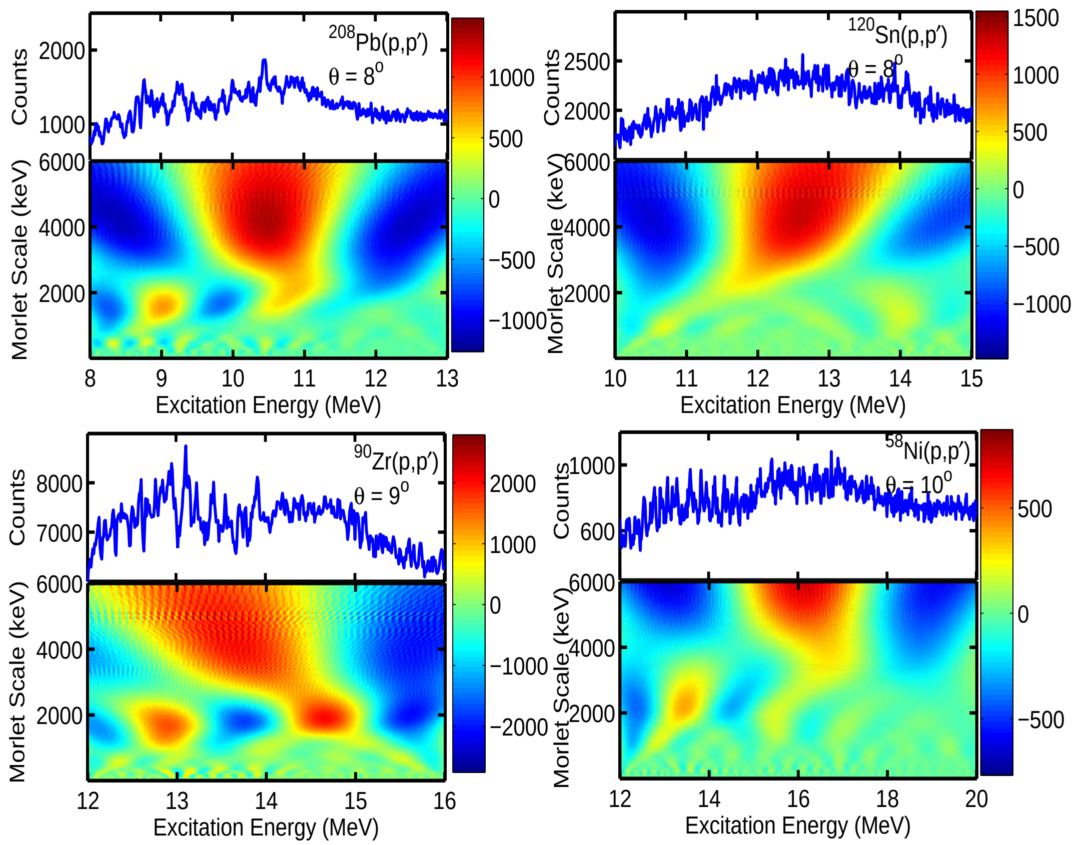

Figure 3.7 Energy spectra for target nuclei ^{208}Pb, ^{120}Sn, ^{90}Zr, and ^{58}Ni shown in the upper part of each diagram for each nucleus at the maximum of the ISGQR. The corresponding real parts of the complex Morlet complex coefficients are shown underneath each spectrum. Note that blue indicates negative values and red positive values.

^{120}Sn: The dashed line shown on the right hand side of Fig. 3.4 corresponds to the wavelet power for ^{120}Sn at $\theta = 8°$, the maximum of the ISGQR. Again peaks can be seen below a scale of 1 MeV corresponding to positions of peaks in the periodogram where significant power is present. Some structure can be seen at scales above 1 MeV but not as clearly as for ^{120}Pb.

^{90}Zr: The dashed lines shown on the right hand side of Fig. 3.5 show the wavelet power spectra for the ISGQR maximum at $\theta = 9°$ and at two scattering angles beyond. Here again distinct peaks, though somewhat spread out, can be seen below a scale of 1 MeV corresponding to the strength in the periodogram which is also spread out. A clear peak at a scale of approximately 2 MeV is seen at all of the scattering angles measured.

^{58}Ni: The dashed line shown on the right hand side of Fig. 3.6 shows the wavelet power for ^{58}Ni at $\theta = 10°$, the maximum of the ISGQR. Below a scale of 1 MeV a single very broad peak can be identified corresponding to the very spreadout power of the periodogram. Above a scale of 1 MeV no clear peaks can be identified.

In general, it can be pointed out that the wavelet power spectra follow the underlying features of the corresponding periodograms, which in their turn reveal sharp, distinctive, substructure. On inspection, though, of the real coefficients plots obtained from the wavelet analysis, see Fig. 3.7, localization of specific features at particular scales can be easily visualized.

3.3.4 Extraction of energy scales from the ISGQR experimental data

A global analysis of all available experimental data reveals three classes of scales: all nuclei studied so far occupy a range, in the present analysis, of $\Delta E < 300$ keV, termed Class I, which is due to the experimental energy resolution of the spectrum and reflects the fine structure present in each nucleus; Class II energy scales of range 300 keV $\leq \Delta E \leq$ 1000 keV which are called intermediate scales and strongly vary from nucleus to nucleus; Class III energy scales of range $\Delta E > 1$ MeV which identify the gross structure and total width of the ISGQR.

Following the above classification, the various significant energy scales seen in the periodogram and wavelet power spectra shown in Figs. 3.3, 3.4, 3.5 and 3.6 have been extracted and tabulated in Tables 3.2, 3.3, 3.4 and 3.5 for ^{208}Pb, ^{120}Sn, ^{90}Zr and ^{58}Ni, respectively. Dominant Fourier and wavelet energy scales are shown in bold. In order to guide the eye, the various columns of Tables 3.2 – 5 contain the values of scales common to both the Fourier and wavelet analyses and link the persistence of that scale to different scattering angles. More than one scale in a box labeled Fourier indicates that these scales correspond to a single peak in the wavelet power spectrum.

3.4 Analysis of Theoretical Models of the ISGQR

Information concerning energy scales present in the region of the ISGQR in the measured high energy-resolution excitation energy spectra and the localization of these scales has been obtained using the Fourier and Wavelet techniques described in Section 3.3. A successful theoretical description of the ISGQR should yield similar, if not identical, energy scales in the predicted strength distribution of the ISGQR for each of the nuclei examined. A number of theoretical models were examined in [SH04] including Random Phase Approximation (RPA), Second RPA (SRPA), Extended Time Depended Hartree-Fock (ETDHF), Extended Theory of Finite Fermi Systems (ETFFS) and Quasi-particle Phonon Model (QPM) (see Subsection 2.2.2), each differing in the complexity of the microscopic description. A definite conclusion was reached in [SH04] that the Quasi-particle Phonon Mode (QPM) best reproduced the energy scales extracted from the measured data for ^{208}Pb. In this section the results of the QPM for each of the four target nuclei are examined and the corresponding energy scales extracted. Comparison with energy scales of the experimental data then follows.

Table 3.2 Summary of energy scales extracted for ^{208}Pb at the various different scattering angles

Lab Angle	**Scale**	**Class I** **ΔE < 300 keV**		**Class II** **300 ≤ ΔE ≤ 1000 keV**			**Class III** **ΔE > 1.0 MeV**		
θ = 6°	Fourier	80	**155** **190**		**341**				
	Wavelet		**170**		**370**		**1.65**		**3.37**
θ = 8°	Fourier	138	**190** 233		**366** **512**				
	Wavelet	**110**	**190**		**500**		**1.69**		**3.93**
θ = 10°	Fourier	80	155 185 233		**366** **512**				
	Wavelet		**180**		**512**		**1.52**		3.75
θ = 12°	Fourier	80	189 223		393	640			
	Wavelet		**160**		**350**	**740**	1.47	**2.57**	3.96

Table 3.3 Summary of energy scales extracted for ^{120}Sn at 8° scattering angle

Lab Angle	**Scale**	**Class I** **ΔE< 300 keV**		**Class II** **300 ≤ ΔE ≤ 1000 keV**			**Class III** **ΔE > 1.0 MeV**		
θ = 8°	Fourier	**78**	**155** **284**			**853**			
	Wavelet	**80**	**160** **300**			800	**1.30**	**1.83**	**4.00**

Table 3.4 Summary of energy scales extracted for ^{90}Zr at the various different scattering angles

Lab Angle	**Scale**	**Class I** ΔE< 300 keV		**Class II** 300 ≤ ΔE ≤ 1000 keV			**Class III** ΔE > 1.0 MeV		
θ = 9°	Fourier	**150** 190	**230**	**340**		**730**	**1.28**	**2.56**	
	Wavelet	**160**	**270**		**600**	**900**		**2.00**	
θ = 11°	Fourier	**155**	240				1.28	2.56	
	Wavelet	**160**	**280**			**990**		**2.02**	
θ = 13°	Fourier	**160**	230		**465**				
	Wavelet	**160**	**280**		**540**		**1.90**		

Table 3.5 Summary of energy scales extracted for ^{58}Ni at 10° scattering angle

Lab Angle	**Scale**	**Class I** ΔE< 300 keV		**Class II** 300 ≤ ΔE ≤ 1000 keV			**Class III** ΔE > 1.0 MeV		
θ =10°	Fourier	126 **200** **280**	300	**569**					
	Wavelet	**200**			500		**1.34**	**2.05**	**5.20**

3.4.1 Quasi-particle Phonon Model (QPM) extraction of energy scales

The QPM [SH04b] was applied to each of the four target nuclei ^{208}Pb, ^{120}Sn, ^{90}Zr, ^{58}Ni, and the corresponding microscopic strength distributions obtained. The strength distributions are represented as a series of delta functions in an excitation energy range from low-lying collective states to the top limit of the ISGQR. These were then folded with a Gauss function of FWHM = 50 keV, representing the average experimental energy resolution and were finally put into 10 keV wide bins similar to the experimental data. These mathematical manipulations were done using Matlab tools developed by A. Shevchenko [SH05].

The results of the folding and binning procedures are shown in the second panel down on the left hand side in Figs. 3.8, 3.9, 3.10, and 3.11 for ^{208}Pb, ^{120}Sn, ^{90}Zr and ^{58}Ni, respectively. Shown also in these figures in the top panel on the left hand side are the corresponding experimental energy spectra measured at the maximum of the ISGQR (see Table 3.1).

It is instructive to extract separately the QPM Collective and QPM Non-collective contributions (see Section 2.2.2). These are shown in the same figures in the third and fourth panels down on the left hand side for the Collective and Non-collective smoothed, rebinned, QPM contributions, respectively.

In order to obtain the energy scales associated with the QPM for each of the target nuclei the Fourier and Wavelet procedures that were applied to the experimental data (see Section 3.3) were applied to the theoretical predictions. The corresponding power spectra are shown on the right hand side of Figs. 3.8, 3.9, 3.10 and 3.11 together with the results for the experimental data. Extracted energy scales are given in Tables 3.6, 3.7, 3.8 and 3.9 for ^{208}Pb, ^{120}Sn, ^{90}Zr and ^{58}Ni, respectively.

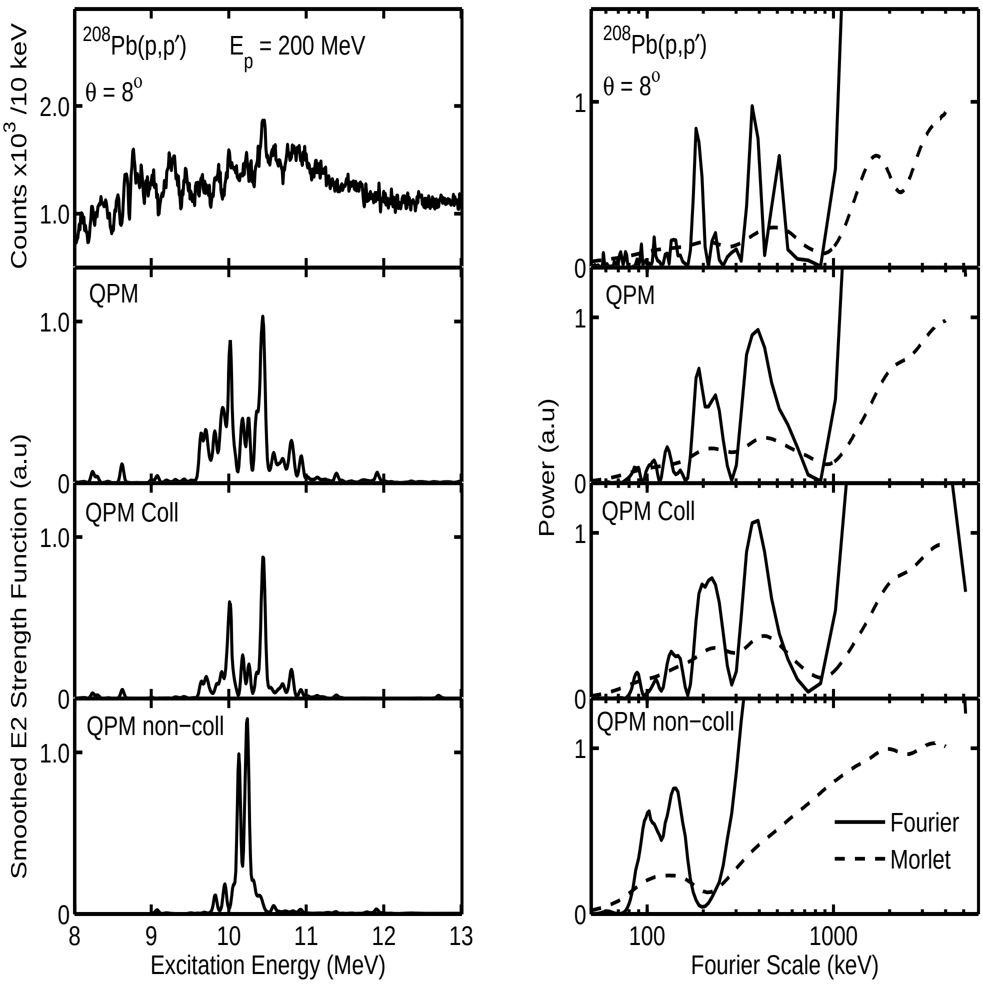

Figure 3.8

Left hand side: Experimental spectrum for ^{208}Pb, QPM prediction of the ISGQR strength function, and its decomposition into collective and non-collective damping distributions.

Right hand side: Corresponding Fourier and wavelet power spectra.

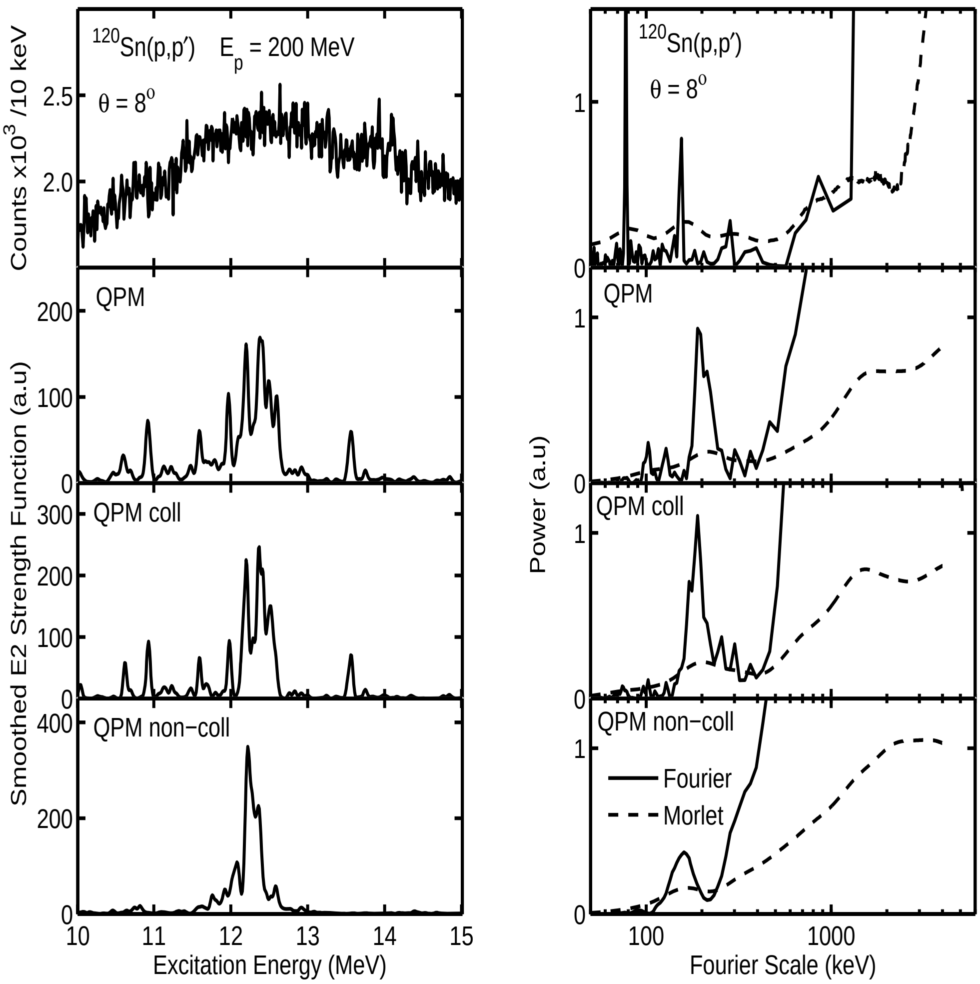

Figure 3.9

Left hand side: Experimental spectrum of ^{120}Sn at $\theta = 8°$ as compared to the QPM result and its decomposition to the collective and non-collective parts.

Right hand side: The corresponding Fourier and wavelet power spectra.

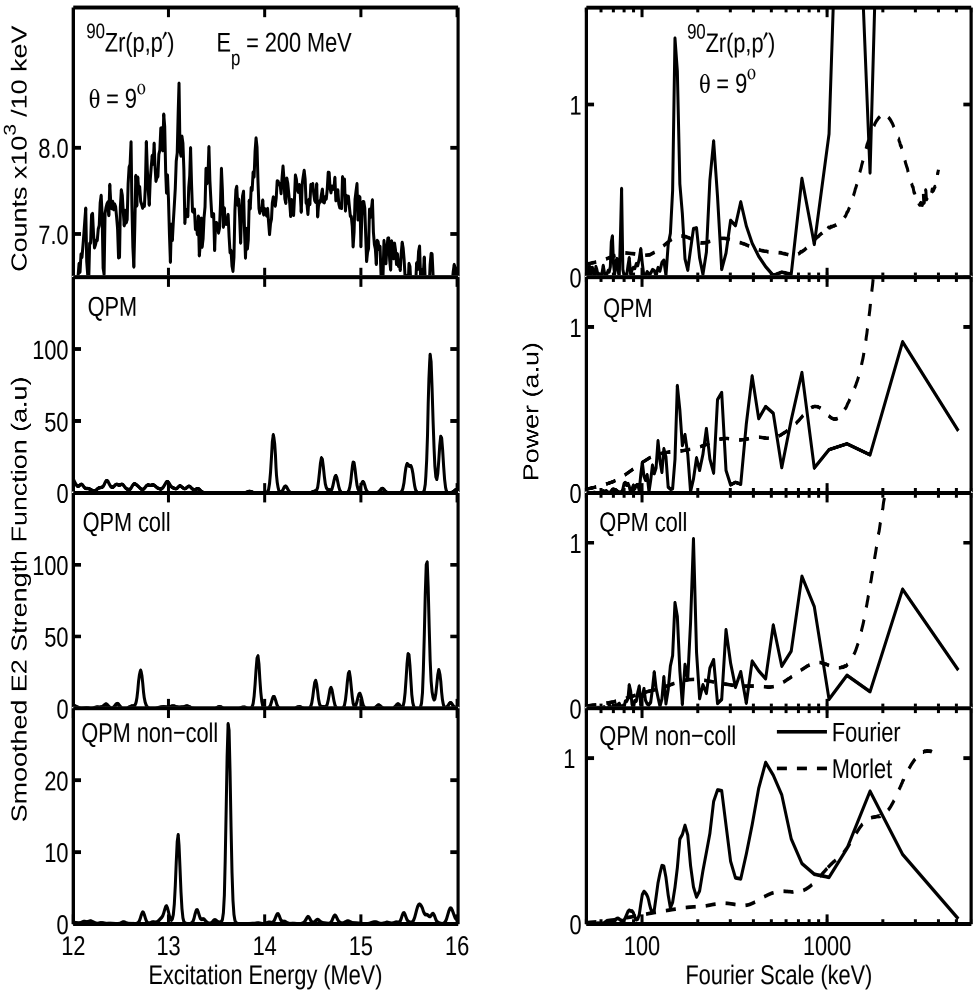

Figure 3.10

Left hand side: Experimental spectrum of ^{90}Zr at $\theta = 9°$ as compared to the QPM result and its decomposition to the collective and non-collective parts.

Right hand side: The corresponding Fourier and wavelet power spectra.

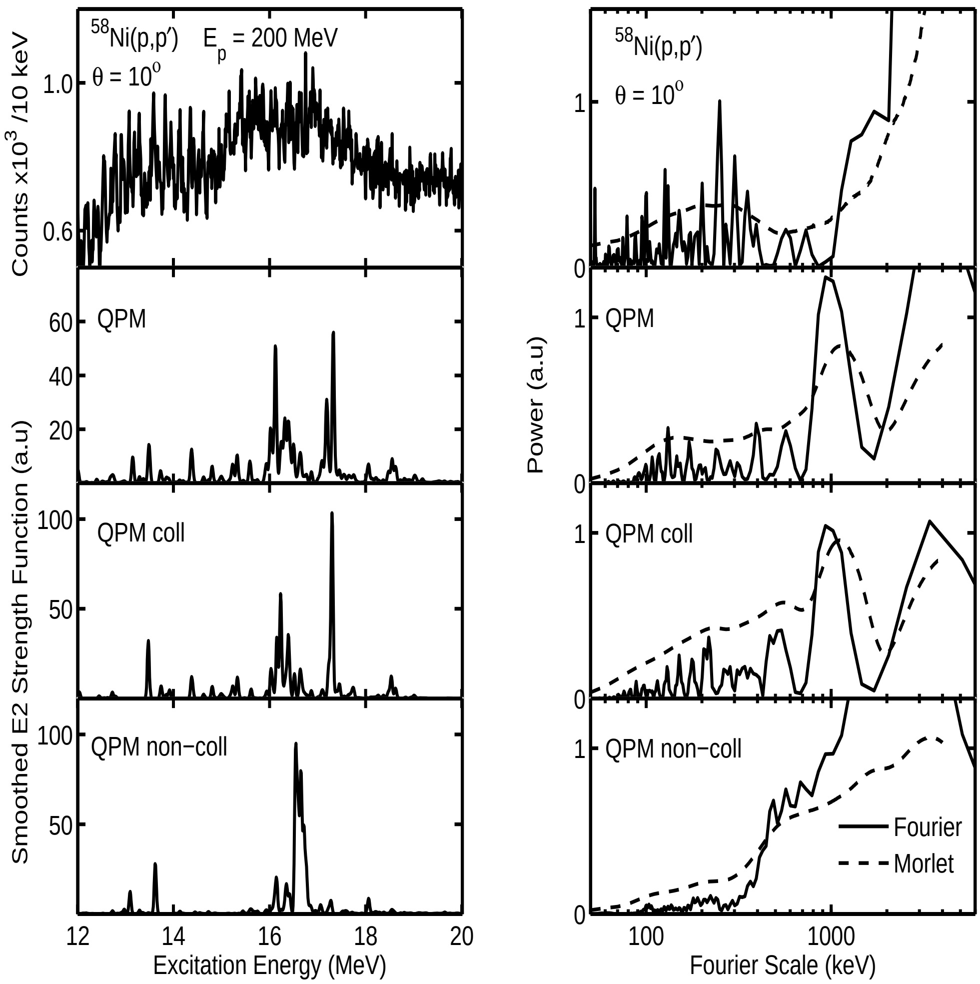

Figure 3.11

Left hand side: Experimental spectrum of ^{58}Ni at θ = 10° as compared to the QPM result and its decomposition to the collective and non-collective parts.

Right hand side: The corresponding Fourier and wavelet power spectra.

Table 3.6 Summary of energy scales observed for ^{208}Pb in comparison with microscopic QPM calculations. Bold indicates the presence of a strong scale and columns indicate correspondence between scales

^{208}Pb	**Scale**	**Class I** **ΔE < 300 keV**				**Class II** **300 ≤ ΔE ≤ 1000 keV**			**Class III** **ΔE >1.0 MeV**		
Expt	Fourier		138	**190**	233		**366** **512**				
	Wavelet	**110**		**190**			**500**		**1.69**		**3.93**
QPM	Fourier	109	138	**190** **220**			**394**	550			
	Wavelet			**205**			**430**			**2.11**	**4.00**
QPM Coll	Fourier	138		**190** **220**			**394**				
	Wavelet			**220**			**420**			**2.01**	**3.78**
QPM Non-coll	Fourier		**100** **140**								
	Wavelet		**120**							1.96	3.36

Table 3.7 Summary of energy scales observed for ^{120}Sn in comparison with microscopic QPM calculations. Bold indicates the presence of a strong scale and columns indicate correspondence between scales

^{120}Sn	**Scale**	**Class I** **ΔE < 300 keV**				**Class II** **300 ≤ ΔE ≤ 1000 keV**			**Class III** **ΔE > 1.0 MeV**		
Expt	Fourier	**78**		**155**	**284**			**853**			
	Wavelet	**80**		**160**	**300**			800	**1.30**	**1.83**	**4.00**
QPM	Fourier			**198** **220**	**299**		365				
	Wavelet			**220**				770	**1.40**		**4.00**
QPM Coll	Fourier			**198**	256 298		370				
	Wavelet			**200**				**750**	**1.45**		**4.00**
QPM Non-coll	Fourier		**165**								
	Wavelet		**160**							**1.74** **3.00**	

Table 3.8 Summary of energy scales observed for ^{90}Zr in comparison with microscopic QPM calculations. Bold indicates the presence of a strong scale and columns indicate correspondence between scales

^{90}Zr	**Scale**	**Class I** **ΔE < 300 keV**				**Class II** **300 ≤ ΔE ≤ 1000 keV**			**Class III** **ΔE > 1.0 MeV**		
Expt	Fourier			**150** 190	**230**	**340**		**730**	**1.28**	**2.56**	
	Wavelet			**160**	**270**		**600**	**900**		**2.00**	
QPM	Fourier			**160**	**270**	**393**	**420**	**730**			
	Wavelet				270			**730**		**3.79**	
QPM Coll	Fourier			**150** **189**	**300**	500		730			
	Wavelet			**170**				840		**3.78**	
QPM Non-coll	Fourier		128	170	269	465					
	Wavelet			180	270	**530**			**1.69**	**3.44**	

Table 3.9 Summary of energy scales observed for ^{58}Ni in comparison with microscopic QPM calculations. Bold indicates the presence of a strong scale and columns indicate correspondence between scales

^{58}Ni	Scale	Class I $\Delta E < 300$ keV				Class II $300 \leq \Delta E \leq 1000$ keV			Class III $\Delta E > 1.0$ MeV		
Expt	Fourier			126 **200** 280	300	**569**					
	Wavelet			**200**			500		**1.34**	**2.05**	**5.20**
QPM	Fourier		**130** 170	240		390	**568**	**930**			**3.41**
	Wavelet		**130**			**420**			**1.14**		**3.96**
QPM Coll	Fourier		150	**176** **217**			**512**	**930**		**3.41**	
	Wavelet			**220**			**550**		**1.11**		**3.96**
QPM Non-coll	Fourier		104	189		487	560	930	**1.28**	**2.47**	
	Wavelet			200			**580**		**1.64**		**3.48**

3.4.2 Comparison of Theoretical and Experimental Energy Scales

For a theoretical interpretation of different classes of scales observed in all the nuclei studied with the application of Fourier and Wavelet analysis, microscopic calculation within the QPM including 2p-2h states at different levels of approximation were investigated. The left hand sides of Figs. 3.8 – 11 show the outcome of E2 strength functions calculated with QPM and its decomposition into collective and non-collective damping while the right hand sides show their corresponding Fourier and Wavelet power spectra. A comparison of the theory with experimental data and a summary of results is presented in Tables 3.6 – 9. Dealing with each target nucleus in turn.

^{208}Pb: Demonstrated in ref. [SH04a] was the correspondence between Wavelet scales extracted from the experimental excitation energy spectrum at $\theta = 8^{o}$, maximum of the ISGQR, and those scales extracted from the theoretical description of the ISGQR provided by the Quasi-particle Phonon Model. This correspondence is, of course, reproduced in the present analysis. Here, though, all energy scales are referenced to the Fourier scale which the complex Morlet produces directly. This is as opposed to the use of the real Morlet wavelet in ref. [SH04] which requires a factor of 0.813 division to yield the equivalent Fourier scale. As seen on the right hand side of Fig. 3.8 the qualitative features of characteristic wavelet scales observed in the experimental data at 190 keV, 500 keV, 1.69 MeV and 3.93 MeV (see Table 3.6) are reproduced in QPM and the QPM Collective component as in ref. [SH04a]. More detailed substructure can, however, be seen in the periodograms for scales below 1 MeV. The QPM Non-collective reveals distinct scales in the Class I region responsible for fine structure.

^{120}Sn: In the case of ^{120}Sn the wavelet and Fourier power spectra for the maximum of ISGQR at $\theta = 8^{o}$ and the QPM predictions are shown on the right hand side of Fig. 3.9. Extracted energy scales are presented in Table

3.7. A Class I energy scale is clearly present in the wavelet power spectrum for the experimental data at approximately 200 keV which also appears in the QPM and the QPM Collective contribution. This is reflected in the Fourier power spectra also. Class II energy scales are not as distinct but there is an indication of a scale at approximately 800 keV appearing in the experimental data and in the QPM and QPM Collective. Gross structure is again seen in Class III scales with scales of approximately 1.40 MeV and 4.00 MeV persisting in the wavelet power spectra for the experimental data and the QPM and QPM Collective. Again a broad distribution of power is seen for the QPM Non-collective with a distinct scale seen only in the Class I region at approximately 160 keV, being very similar to the features seen in the ^{208}Pb QPM Non-collective contribution.

^{90}Zr: Wavelet and Fourier power spectra are shown on the right hand side of Fig. 3.10 for ^{90}Zr for the maximum of the ISGQR at $\theta = 9^{\circ}$ and the QPM predictions. Extracted energy scales are presented in Table 3.8. A broad distribution of wavelet power can be seen for the experimental, QPM and QPM Collective but with the aid of the corresponding coefficient plots energy scales can be more easily extracted. A Class I scale at approximately 160 keV can be identified in the experimental data which persists in the QPM and QPM Collective. An important Class II scale at approximately 800 keV can be identified in the experimental data, QPM and QPM Collective with the indication of another scale at approximately 400 keV. Large scale Class III structure can again be identified at approximately 2 MeV and 4 MeV. A lot of detail can be seen in the Fourier power spectra with generally a very good correspondence between the experimental data, QPM and QPM Collective. The QPM Non-collective is again very reminiscent of ^{208}Pb and ^{120}Sn.

^{58}Ni: The corresponding power spectra for ^{58}Ni measured at the maximum of the ISGQR $\theta = 10^{\circ}$ and for the QPM predictions are shown on the right hand side of Fig. 3.11. Extracted energy scales are presented in Table 3.9.

Below 1 MeV the wavelet power spectra are broad and generally featureless but specific scales can be extracted with the aid of the corresponding coefficient plots. Class I scales can be identified at approximately 200 keV and show a correspondence between the experiment and the QPM and QPM Collective. A Class II scale shows up in the QPM and QPM Collective at approximately 500 keV and is weakly present in the experimental wavelet power spectrum. The very prominent scale at approximately 1 MeV in the QPM and QPM Collective could be associated with a weak scale in the experimental data just above 1 MeV. Large scale Class III structure is seen at 2 MeV and 5 MeV in the experimental data with some correspondence seen in the QPM predictions. The Fourier power spectra show a lot of detail below 1 MeV with some good general correspondence between the experiment, QPM and QPM Collective. Again the QPM Non-collective shows features present in the other target nuclei.

Generally, one could say that Fourier analysis reveals energy scales within the ISGQR region in a far more detailed way than that achieved by the wavelet analysis but at the expense of localization as is done in wavelet coefficients plot. Morlet power spectrum represents a smoothed version of the Fourier power spectrum, confirming the correspondence between different analytical approaches.

3.5 Reconstruction of excitation energy spectra

Reconstruction of the original experimentally-measured excitation energy spectrum in the region of ISGQR allows more insight to be gained as to the nature of the different energy scales. Large scales of Class III represent the overall width of the ISGQR while Classes II and I bring out specific finer details associated with the damping mechanisms. The Inverse Fourier Transform is a long standing reliable technique for the reconstruction of the original spectrum.

Typical, though, in the case of Wavelet analysis the Discrete Wavelet Transform (DWT) has been used which allows an exact reconstruction, as does the Inverse

Fourier Transform. The drawback here is that reconstruction for the DWT is constrained to powers of two within the energy scales. As an alternative, spectrum reconstruction has been developed from the Continuous Wavelet Transform (CWT), thus allowing a much greater flexibility to include only specific scales.

3.5.1 Inverse Fourier Transform spectrum reconstruction

By way of example and since it is the most extensively studied, spectrum reconstruction for ^{208}Pb is presented in detail. This spectrum reconstruction was achieved by using an existing interactive Fourier-transform-based data processing programme, SignProc [CO05]. The resulting frequency power-spectrum for the ISGQR region in ^{208}Pb was calculated. It is, however, more useful for our purpose to display the inverse of the frequency power-spectrum as wavelength or energy scale. The bottom part of Fig. 3.12 shows the wavelength power-spectrum which is identical to the periodogram shown in Fig. 3.8 (upper right) from which the Fourier energy scales are directly determined.

A low-pass filter was applied to the complex Fourier coefficients (guided by the frequency power-spectrum) with an Inverse Fourier transform yielding the largest energy-scales structures (Class III) as shown in middle box of Fig. 3.12. Note that the original ISGQR data minus the mean is produced as an oscillation around zero. By adding the mean value of the original data to the oscillation in the middle box of Fig. 3.12 a direct comparison with the data is possible as provided by the solid block line in the top part of Fig. 3.12.

Similarly, Class II coefficients can be extracted for spectrum reconstruction by using this time a band-pass filter. The results are shown in Fig. 3.13. It is, however, more useful to superimpose Class II structures on top of those generated by the largest energy scales Class III. This can be done using a low-pass filter to extract both Class III and Class II Fourier coefficients, the results of which are shown at the top part of Fig. 3.13 as the black solid line.

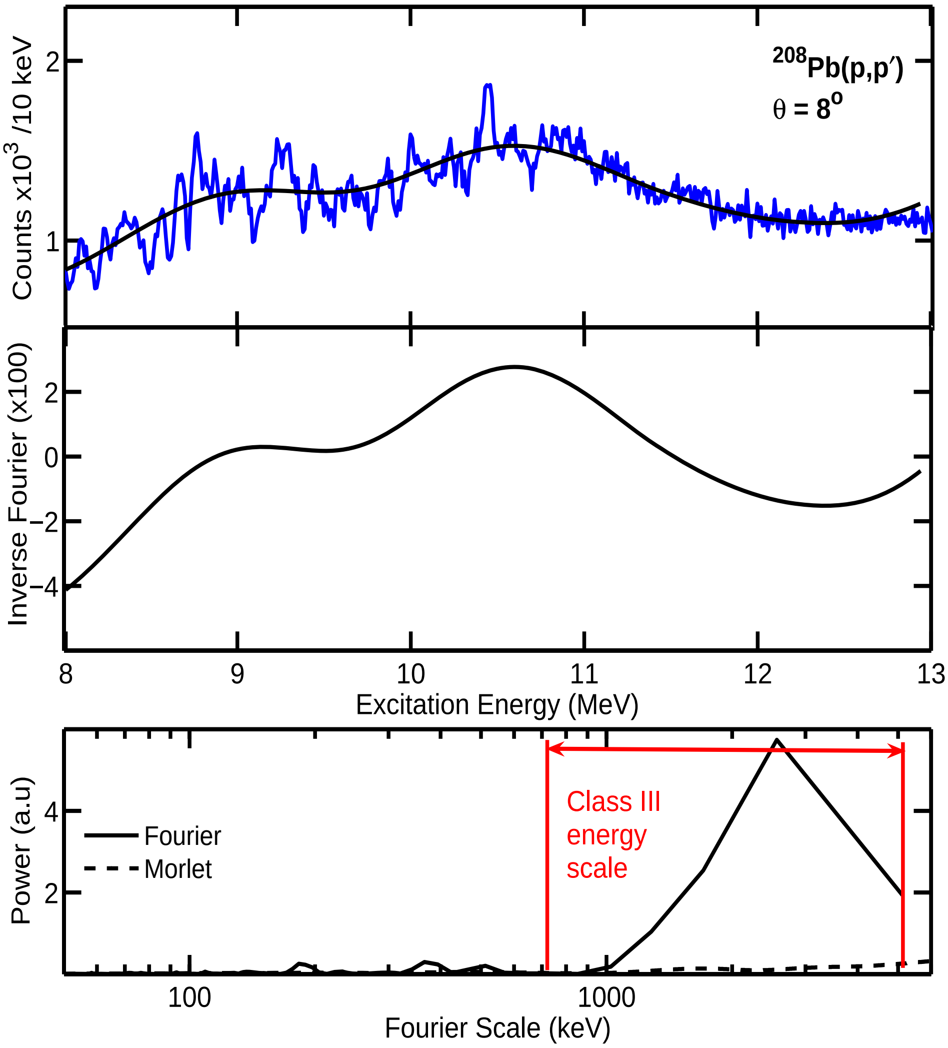

Figure 3.12 Reconstructed energy spectrum using the Inverse Fourier Transform (middle box) with the application of low-pass filter on the Fourier frequency coefficients for Class III energy scales. The original ^{208}Pb GQR excitation energy spectrum in the region 8 to 13 MeV is shown in the upper box (blue) and the corresponding scale region indicated between the arrows in the lower box.

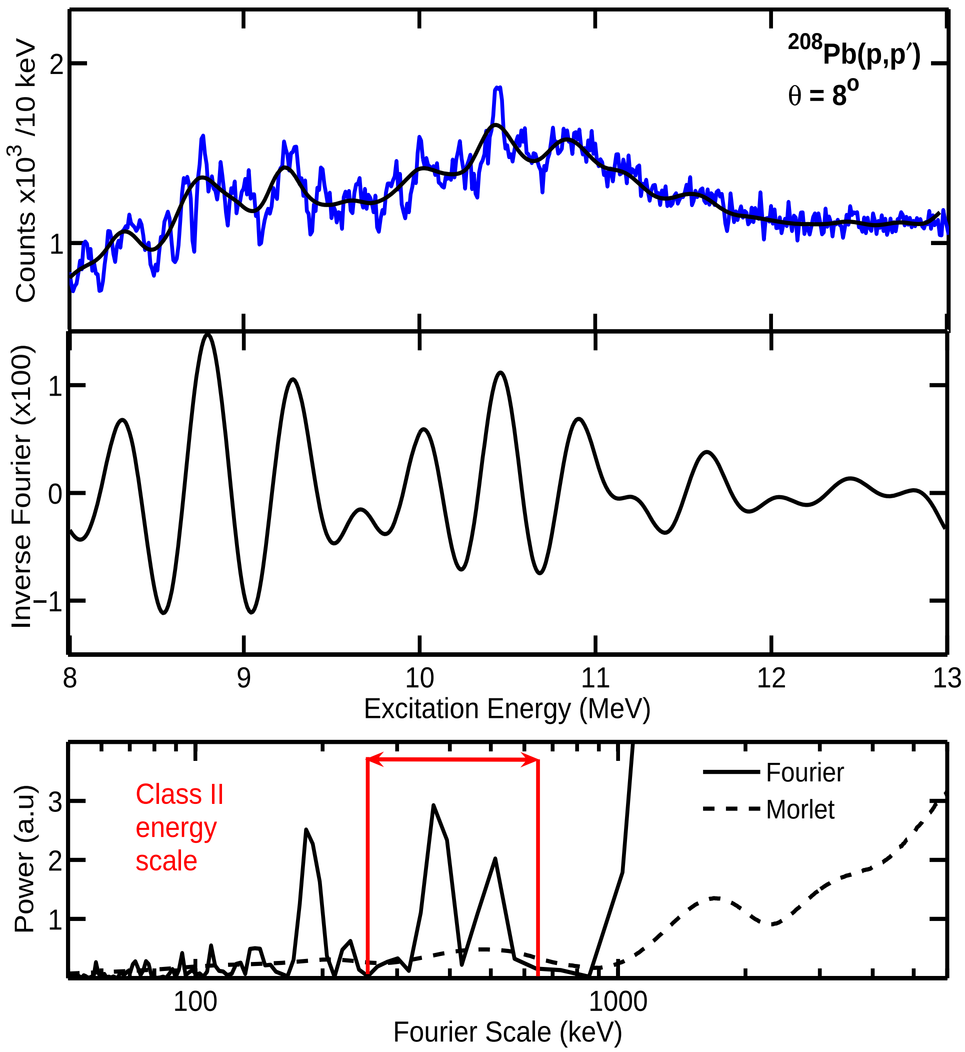

Figure 3.13 Reconstructed energy spectrum using the Inverse Fourier Transform (middle box) and a band-pass filter on the Fourier frequency coefficients for Class II energy scales. The original ^{208}Pb GQR excitation energy spectrum in the region 8 to 13 MeV is shown in the upper box (blue) and the corresponding scale region indicated between the arrows in the lower box.

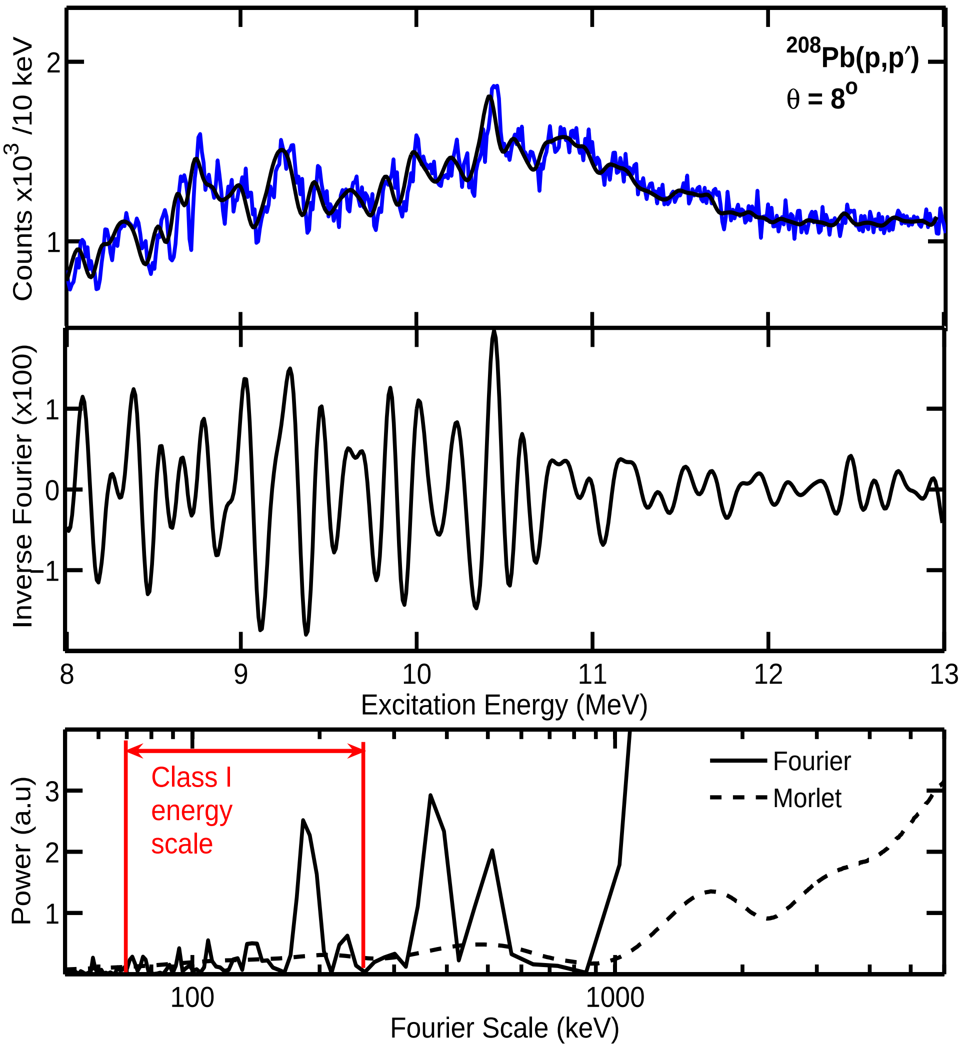

Figure 3.14 Reconstructed energy spectrum using the Inverse Fourier Transform (middle box) and a high-pass filter on the Fourier frequency coefficients for Class I energy scales. The original ^{208}Pb GQR excitation energy spectrum in the region 8 to 13 MeV is shown in the upper box (blue) and the corresponding scale region indicated between the arrows in the lower box.

Finally, Class I structures are reconstructed by the application of a high-pass to the Fourier coefficients, the results of which are displayed in Fig. 3.14. Again it is useful to superpose the Class I structures on the gross structure generated by Class II and Class III energy scales. This is shown at the top part of Fig. 3.14.

3.5.2 Continuous Wavelet Transform spectrum reconstruction

Specific features in the original excitation energy spectrum can be identified by inspection of the wavelet coefficients plot of energy scale *versus* excitation energy. Here, a red area corresponds to large positive coefficients and a blue area to large negative, indicating the position of a peak maximum and peak minimum, respectively. It is, however, instructive to reconstruct a spectrum component by summing the coefficients belonging to a certain energy scale down to the excitation energy axis. The resulting oscillatory structure around zero is then scaled back to the measured spectrum. In order to illustrate this procedure and by way of example this was done for the case of ^{208}Pb. Figure 3.15 shows the reconstruction for the largest scale in Class III at 3.93 MeV (see Table 3.6). The range of summation of coefficients is indicated in the bottom part of Fig. 3.15 with the resulting sum of coefficients shown in the middle part of Fig. 3.15.

After scaling the summed coefficients up to the experimental spectrum a broad, single peak, shown by the black line is plotted over the original spectrum, blue line, in the top part of Fig. 3.15. The procedure is repeated for the successively smaller scales identified (see Table 3.6) in Figs. 3.16, 3.17 and 3.18, each time adding to all previously summed coefficients before scaling to the measured spectrum. Thus, by Fig 3.18 a complete spectrum reconstruction is achieved using all of the coefficients indicated.

3.5.3 Discrete Wavelet Transform spectrum reconstruction

It is not required to repeat the DWT reconstruction again since it has been studied in detail in ref. [SH04b] and this is mentioned here for comparison with our own methods used, that is, Inverse Fourier and Continuous Wavelet transforms. See Appendix B for a full discussion of DWT spectrum reconstruction.

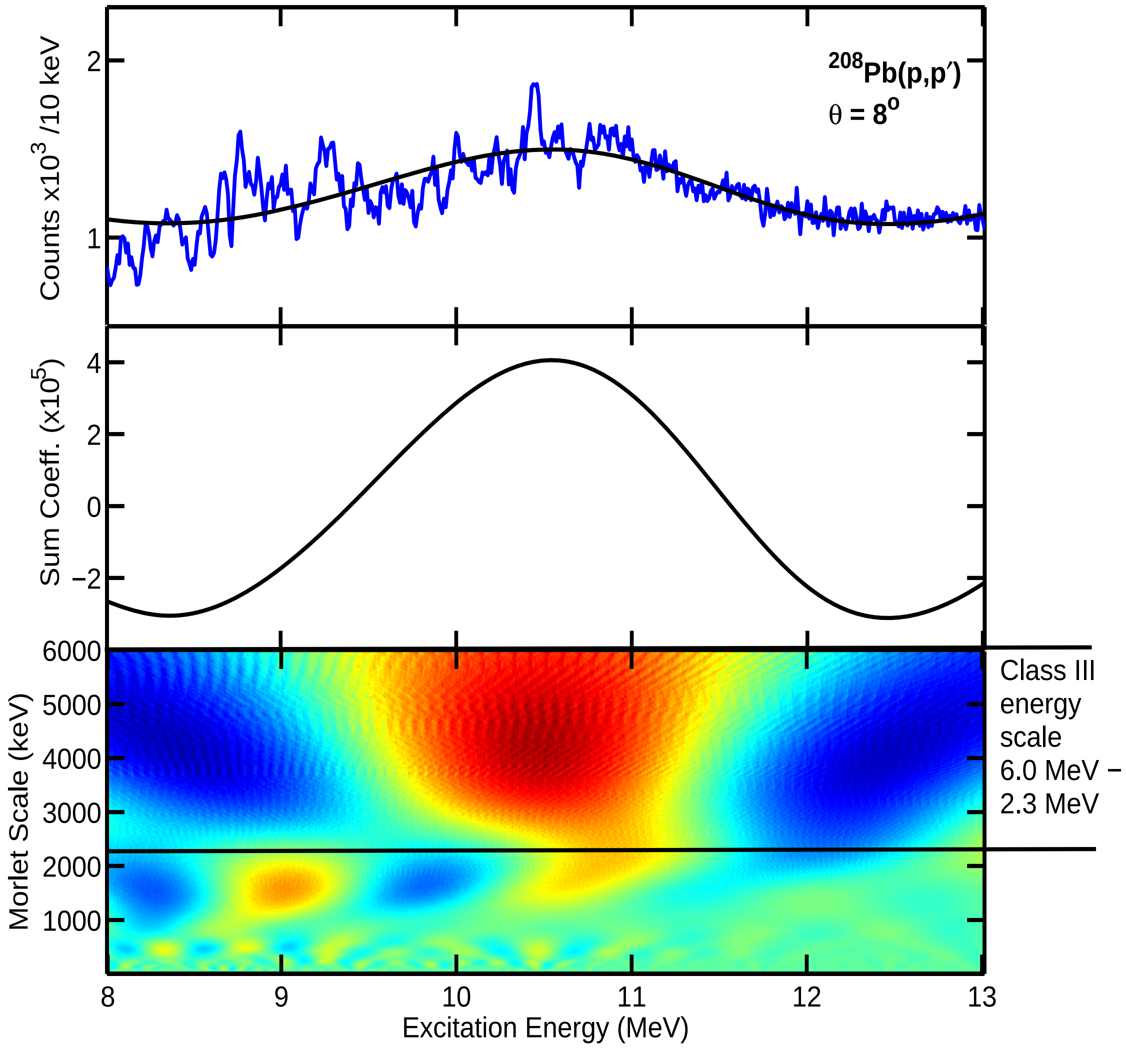

Figure 3.15

Top: Class III energy scale showing the reconstruction, indicated with a black line.

Middle: Sum of the real coefficients between the limits shown in the plot.

Bottom: The region of largest energy scale between 2.3 MeV and 6.0 MeV indicated on the plot of real coefficients only produced using the Complex Morlet wavelet.

.

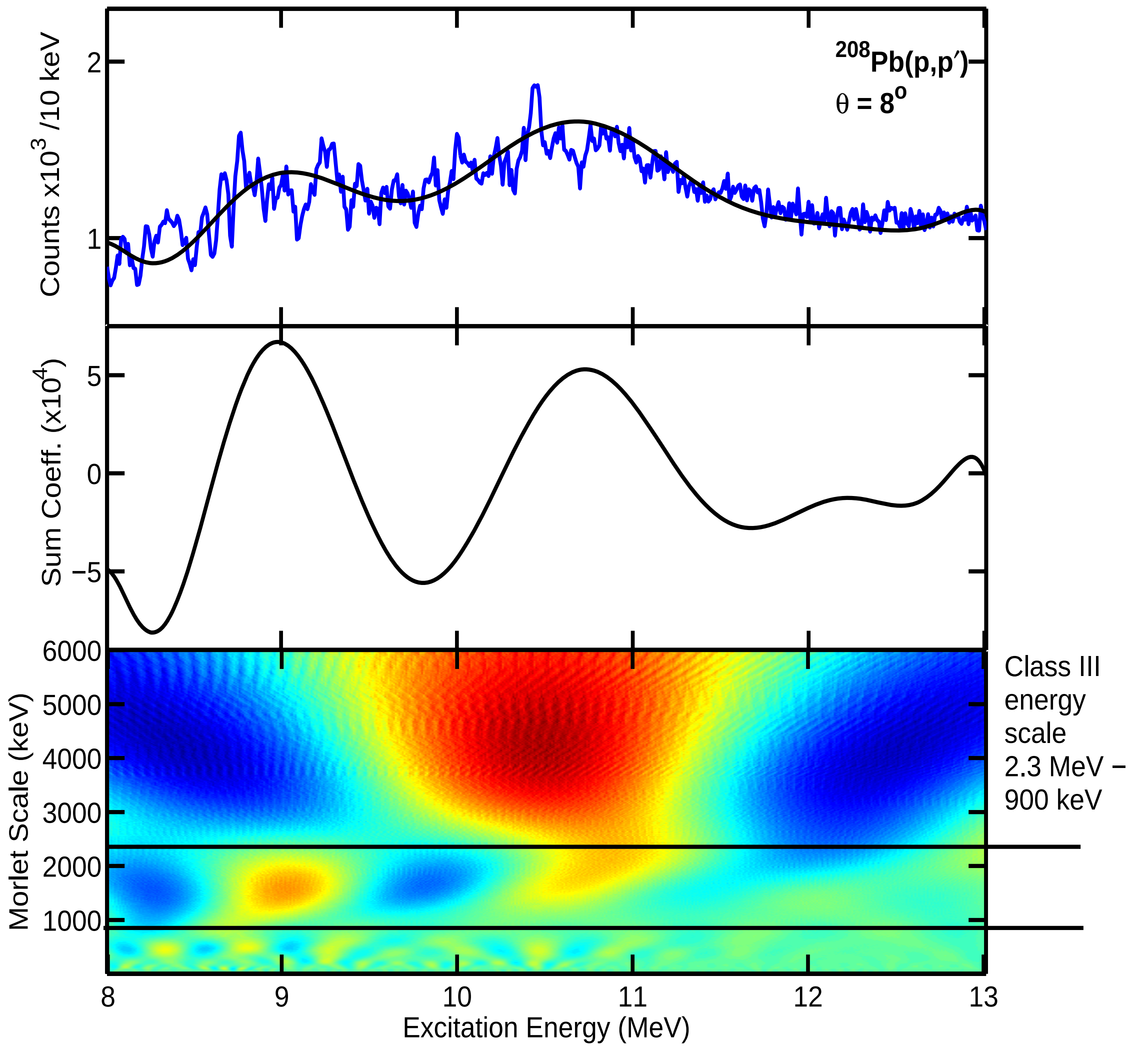

Figure 3.16

Top: Class III energy scales showing the reconstruction after adding the summed Class III coefficients of Fig. 3.15 indicated with a black line.

Middle: Sum of the real coefficients between the limits shown in the plot.

Bottom: The region of second largest energy scale between 990 keV and 2.3 MeV indicated on the plot of real coefficients only produced using the Complex Morlet wavelet.

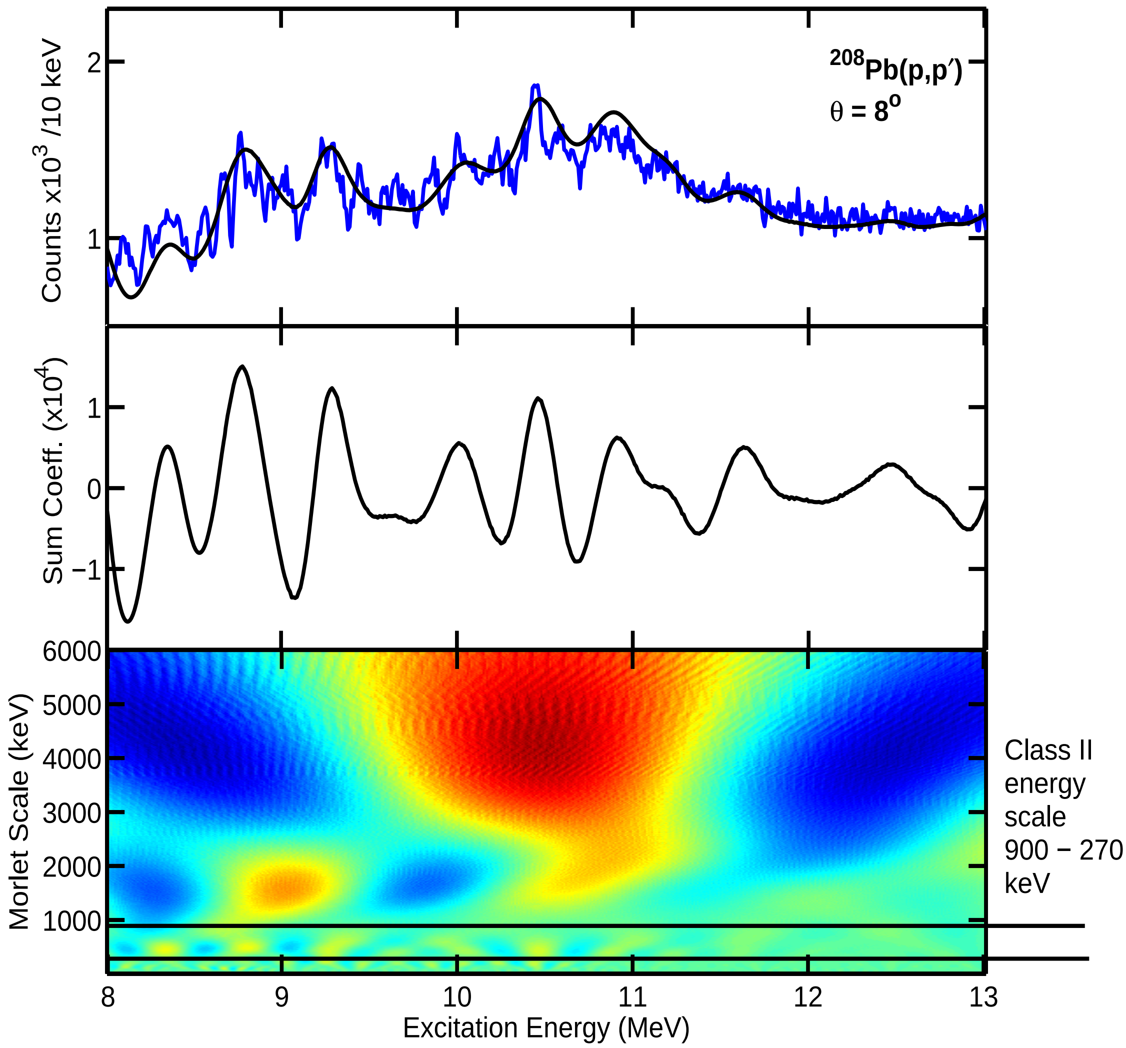

Figure 3.17

Top: Class II energy scale showing the reconstruction after adding the Class III coefficients of Figs. 3.15 and 3.16 indicated with a black line.

Middle: Sum of the real coefficients between the limits shown in the plot.

Bottom: The region of medium energy scale between 270 keV and 990 keV indicated on the plot of real coefficients only produced using the Complex Morlet wavelet.

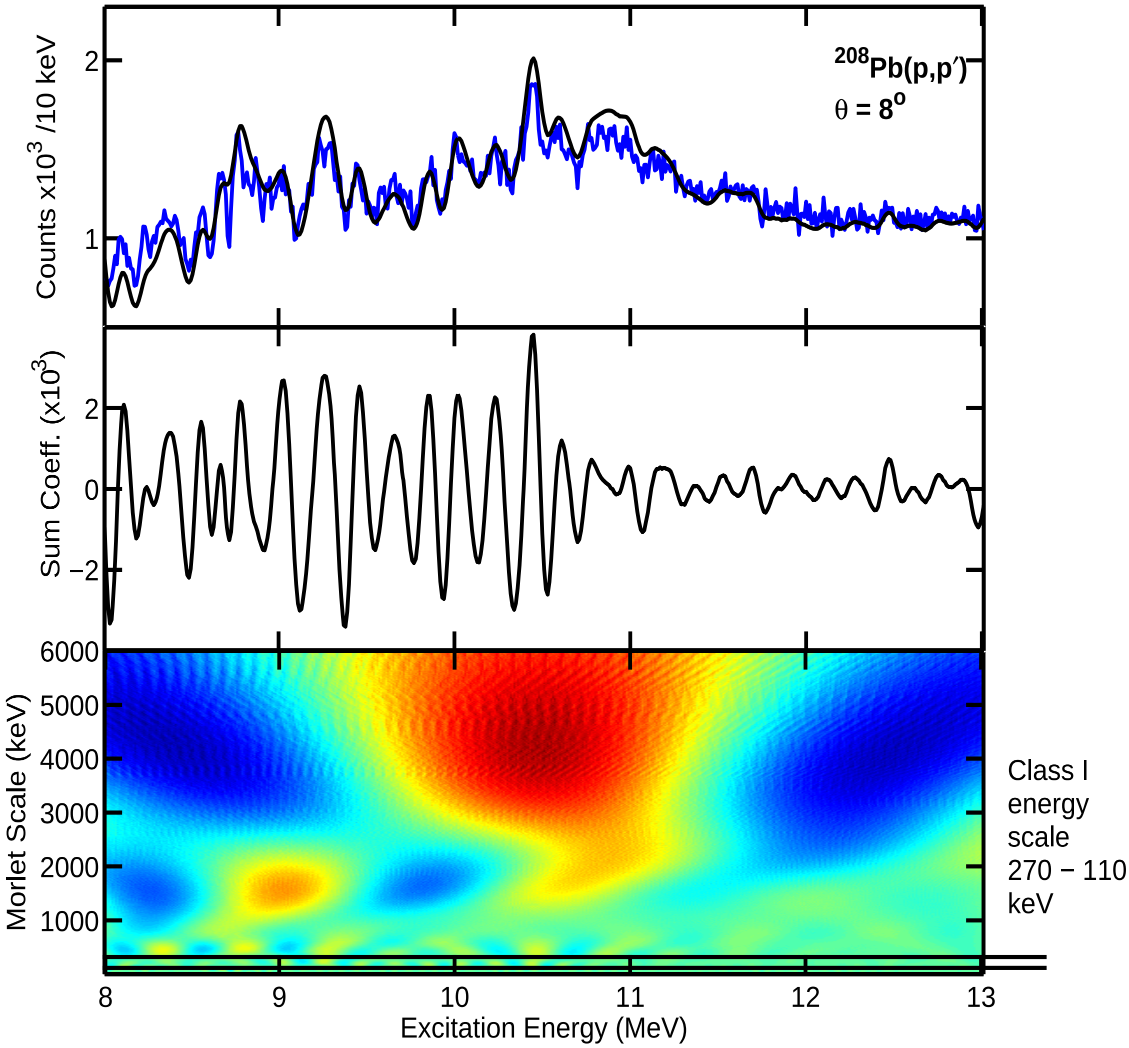

Figure 3.18

Top: Class I energy scale showing the reconstruction after adding the summed Class II coefficients of Fig. 3.17 and the summed Class III coefficients of Fig. 3.15 and 3.16 indicated with a black line.

Middle: Sum of the real coefficients between the limits shown in the plot.

Bottom: The region of small energy scale between 110 keV and 270 keV indicated on the plot of real coefficients only produced using the Complex Morlet wavelet.

3.5.4 Discussion of spectrum reconstruction results

Spectrum reconstruction allows further insight to be gained as to the importance of the various energy scales identified. Dealing with each class of energy scale in turn.

Class III: The Class III energy scales are associated with the gross structure of the ISGQR and for ^{208}Pb span a range of approximately 900 keV to 6.0 MeV. Inverse Fourier reconstruction is shown in Fig. 3.12, Continuous Wavelet Transform (CWT) reconstruction is shown in Figs. 3.15 and 3.16, and Discrete Wavelet Transform (DWT) decomposition in Fig. 5.15 of Appendix B. The CWT shows the clearest reconstruction. Here, for the largest scale of 3.93 MeV (see Table 3.6) with a range of CWT coefficients spanning 2.3 to 6.0 MeV (see bottom part of Fig. 3.15) the resulting single peak average through the experimental spectrum is shown in the top part of Fig. 3.15, displaying a width (FWHM) of the ISGQR in ^{208}Pb of approximately 2 MeV. A second smaller scale associated with Class III is identified in the bottom part of Fig. 3.16 with a range of 900 keV to 2.3 MeV, centred at 1.69 MeV (see Table 3.6). This yields two smaller width peaks (each approximately 900 keV wide) centred at an excitation energies of 9 and 10.8 MeV (see middle part of Fig. 3.16). When combined with the largest scale of Fig. 3.15 a good representation of the average structure of the experimental spectrum is seen in the top part of Fig. 3.16. Of course, by inspection, very little of the second scale at 1.69 Mev is seen above $E_x \approx 11.3$ MeV (bottom part Fig. 3.16).

Alternatively, spectrum reconstruction can be achieved using the Inverse Fourier Transform as shown in Fig. 3.12. Here, scales above 1 MeV are not easily distinguished separately as seen in the bottom part of Fig. 3.12. The reconstruction, though, top part of Fig. 3.12, yields a result very similar to both Class III scales identified using the CWT method (Fig. 3.16).

Turning now to the DWT decomposition, the bottom right hand side of Fig. 5.15 in Appendix B with boxes labeled D7, D8 and D9 are associated with the largest scales discussed previously. However, as can be seen, there is no control over the range of scales that can be included in the DWT decomposition. This severely limits the procedure. It should be noted that the range of scales identified in Fig. 5.15 of Appendix B need a factor of 0.813 divisor in order to produce an equivalent Fourier scale.

Class II: The intermediate energy scale known as Class II is presented in the bottom part of Fig. 3.17 within a range of 270 – 900 keV and it is centred at 500 keV (see Table 3.6). This energy scale produces about seven smaller width peaks (each approximately, 200 keV wide) centred at excitation energies of 8.5, 8.9, 101, 10.5, 10.9, 11.5 and 12.3 MeV, respectively (see middle part of Fig. 3.17).

Likewise, the Inverse Fourier Transform reconstruction shown in Fig. 3.13 yields a similar figure as in the Class II energy scale identified using CWT method (see top part of Fig. 3.17). In order to compare this result with DWT decomposition, the middle right hand side of Fig. 5.15 in Appendix B is considered, with box labeled D5 which is associated with the intermediate energy scale discussed above.

Class I: The same procedures apply to the Class I energy scales which are associated with the experimental energy resolution of the spectrum. This is illustrated in the bottom part of Fig. 3.18 within a range of 110 – 270 keV, centred at 190 keV (see Table 3.6). This yields a number of peaks of narrow width (see middle part of Fig 3.18).

When combined with the summed of Class III and Class II coefficients of Fig. 3.17 full reconstruction can be identified as shown in the top part of Fig. 3.18 with the black solid line.

Inverse Fourier Transform reconstruction of Fig. 3.14 for Class I energy scales produces a similar spectrum to the CWT as can be seen in the middle part of Fig 3.18. The DWT decomposition is depicted in the middle right hand side of Fig. 5.15 in Appendix B with box labeled D4 associated with the smallest scales discussed with the use of both Inverse Fourier and CWT reconstruction.

In general, one can see that the use of CWT method of reconstruction allows an exact range of scales to be identified and it is more versatile.

CHAPTER 4

CONCLUSIONS

The Isoscalar Giant Quadrupole Resonance (ISGQR) region for the closed-shell nuclei ^{208}Pb, ^{120}Sn, ^{90}Zr and ^{58}Ni has been investigated using inelastic proton scattering at 200 MeV. Energy scales have been extracted by applying both Fourier and Wavelet analysis techniques. In both cases, standard data preparation was applied to the input data set and was found to be essential in order to minimise end effects. A global analysis of the experimental data reveals three classes of scales; all nuclei studied so far exhibit a scale below 300 keV (Class I scales), two or three scales between about 300 keV and 1000 keV strongly varying from nucleus to nucleus (Class II scales) and a scale of several MeV reflecting the total width of the resonance (Class III scales).

In order to reveal the physical nature of observed scales, a comparison to the state-of-the-art Quasi-particle Phonon Model (QPM) predictions was made, in which different damping mechanism could be disentangled. Thus, within the QPM, collective and non-collective damping were treated separately and the application of the Fourier and Wavelet analysis indicated different results for these two mechanisms. The collective damping, coupling to low-lying collective states, was found to be responsible for Class II and Class III scales, confirming the commonly accepted hypothesis that the collective mechanism is dominant in the damping process. Furthermore, several scales in the intermediate energy range (Class II) are always found but with considerable variation between the different nuclei studied. On the other hand, the characteristic Class I scales result from damping to a 'sea' of complex 2p-2h states and reflect the inherent experimental resolution of approximately 50 keV (FWHM).

The Fourier transform provides a more detailed set of energy scales in comparison to the Wavelet analysis. This, however, was at the expense of localisation of the scale within the energy spectrum. It should be noted that in the present analysis a complex Morlet wavelet was used to yield an equivalent Fourier scale. Here, the real part of the resulting complex coefficients when displaced on a two dimensional plot of energy scale *versus* excitation energy allows directly visualisation of the regions of importance of the various scales within the measured excitation energy spectra. As a result, it could be seen that energy scales identified at a scattering angle corresponding to the maximum of the ISGQR became less important at smaller and larger scattering angles where data were available for a particular nucleus.

In order to gain further insight into the role of the different energy scales, reconstruction of the original experimental ISGQR was achieved using the Inverse Fourier transform after applying appropriate filters to isolate the Class I, II or III energy scales. This was extended further using an algorithm applied to the coefficients produced by the Continuous Wavelet Transform (CWT). Both approaches produced similar results. The advantage though of the CWT was that specific scales showed regions of importance within the coefficient plots. On the other hand, spectrum reconstruction from the Discrete Wavelet Transform (DWT) has a severe limitation of powers of 2 within energy scales, obviously limiting the range of scales that can be selected for spectrum reconstruction.

BIBLIOGRAPHY

[AB96] Y. Abe, S. Ayik, P.-G. Reinhard and E. Suraud, Phys. Rep. **275,** 49 (1996).

[BA47] G. C. Baldwin and G. S. Klaiber, Phys. Rev**. 71**, 3 (1947).

[BE79] G. F. Bertsch, Nature **280**, 23 August (1979).

[BE81] Bertrand *et al.*, Nucl. Phys. A **354**, 126c (1981).

[BE83] G. F. Bertsch, P. F. Bortignon and R. A. Broglia, Rev. Mod. Phys. **55**, 287 (1983).

[BE99] C. Bertulani and V. Ponomarev, Phys. Rev.C **321**, 139 (1999).

[CA90] W. Cassing and U. Mosel, Prog. Part. Nucl. Phys. **25**, 235 (1990).

[CA02] J. Carter *et al*., Research Proposal to iThemba LABS: *Fine structure of giant resonances in closed-shell nuclei as a test of the doorway Picture*, September, 2002.

[CO05] G. R. J. Cooper, Signproc: *a program for filtering magnetic profile data.* South African Geophysical Review, V.**3**, 69-75, 1999.

[GE00] B. George, L. Narici and E. Beckenstein, *Fourier and wavelet Analysis*, Springer - Verlag, New York, 2000.

[IT05] M. Itoh, RCNP, Osaka University, Private Communication, 2005.

[JO92] Jones and Barlett, *Wavelet and Their Applications*, edited by R. Coifman, Boston, 1992.

[KA04] Y. Kalmykov, PhD Thesis, D17, TU Darmstadt, 2004.

[KA97] S. Kamerdzhiev *et al.*, Phys. Rev. C **55**, 2101 (1997).

[KA94] G. Kaiser, *A Friendly Guide to Wavelets*, Boston, Birkhauser, 1994.

[KU81] G. Kuhner *et al*., Phys. Lett. B **104**, 189 (1981).

[LA00] D. Lacroix *et al.*., Phys. Lett. B **479**, 15 (2000).

[LA01] D. Lacroix, S. Ayik and P. Chomaz, Phys. Rev. C **63**, 064305 (2001).

[LI91] J. Lisantti *et al.*, Phys. Rev. C **44**, R1233 (1991).

[MA06] The Mathworks, inc., *Matlab,The Language of Technical Computing*, Version, 7.2.0.232 (R 2006a), Copyright, 1984-2006.

[PO93] V. Yu. Ponomarev and V. V. Vonorov, *Looking inside Giant Resonance fine Structure*, JINR communication, E **4**-93-334, Dubna, (1993).

[RE94] P.-G. Reinhard and C. Toepffer, Int. J. Mod. Phys. E **3,** 435 (1994).

[RI05] A. Richter, *Giant resonances – experiments at highest resolution; wavelets and scales*, Prog. Part. Nucl. Phys. **55,** 387–396 (2005).

[RO70] D. Rowe, *Nuclear Collective Motion*, Methuen, London, 1970.

[SH04a] A. Shevchenko *et al*., Phys. Rev. Lett. C **93,** 122501 (2004).

[SH04b] A. Shevchenko, PhD Thesis, D17, T U Darmstadt, 2004.

[SH05] A. Shevchenko, Private Communication, Matlab routines, 2005.

[VO05] P. Von Neumann-Cosel, *Proceedings of the International Workshop XXXII on Gross properties of Nuclei and Nuclear Excitations*, Hirschegg, Austria, January 11-17, 189-196 (2004).

[VA87] A. Van der Woude, Giant resonances, Prog. Part. Nucl. Phys. **18**, 217-293 (1987).

[VO83] V. V. Voronov and V. G. Soloviev, Particles and Nuclei, **14,** 1380 (1983).

[WE67] P. D. Welch, *The use of fast Fourier transform for the estimation of power spectra: A method based on time averaging over short, modified Periodograms,* IEEE Trans. Audio Electroacoustics, Vol. AU-**15**, 70-73 (1967).

APPENDIX A

A Copy of Physical Review Letters publication [SH04a].

APPENDIX B

An extract from PhD thesis of A. Shevchencko on Discrete Wavelet Transform spectrum reconstruction [SH04b].